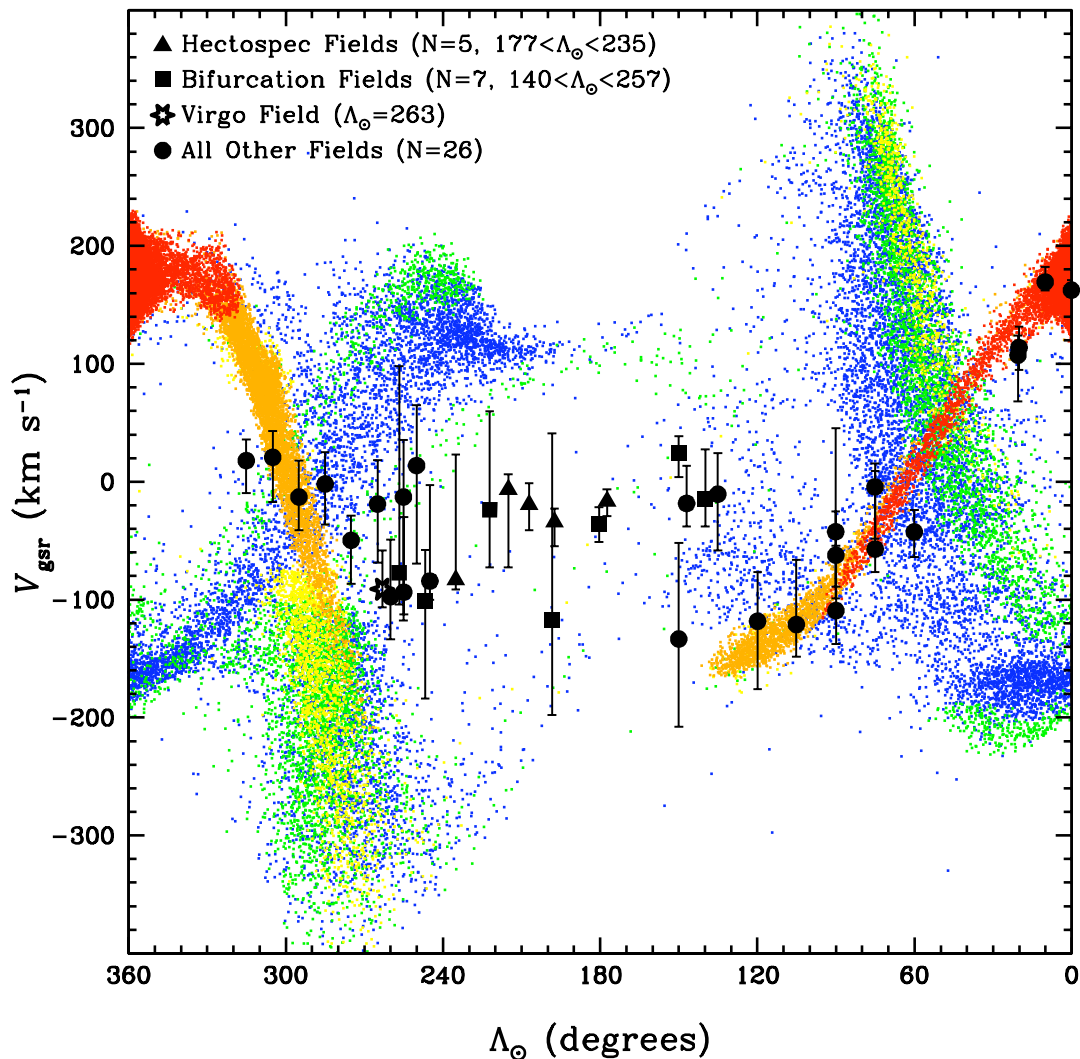**Figure 5.24:** Comparison of oblate halo model and primary velocity peaks. The Galactic standard of rest radial velocities for the oblate halo model stars that satisfy the distance cut (described in Section 5.2.2.3) are shown as a function of their Sgr longitude. The model stars are color-coded as before to indicate on which orbit they became unbound from the core of Sgr. The black data points are plotted at the $(\Lambda_\odot, V_{peak})$ values for the 39 fields in our survey. The five solid black triangles with $177° < \Lambda_\odot < 235°$ represent the Hectospec fields. The seven solid black squares with $140° < \Lambda_\odot < 257°$ represent the fields along the northern hemisphere bifurcation in the stream (Belokurov et al., 2006). The black star at $\Lambda_\odot = 263°$ denotes the Virgo field discussed in Chapter 4. The 26 solid black circles represent the remaining fields. Asymmetric error bars (as discussed in Section 5.1) are included for each observation. The peak velocities and the lengths of the error bars are listed for every field in Table 5.2.
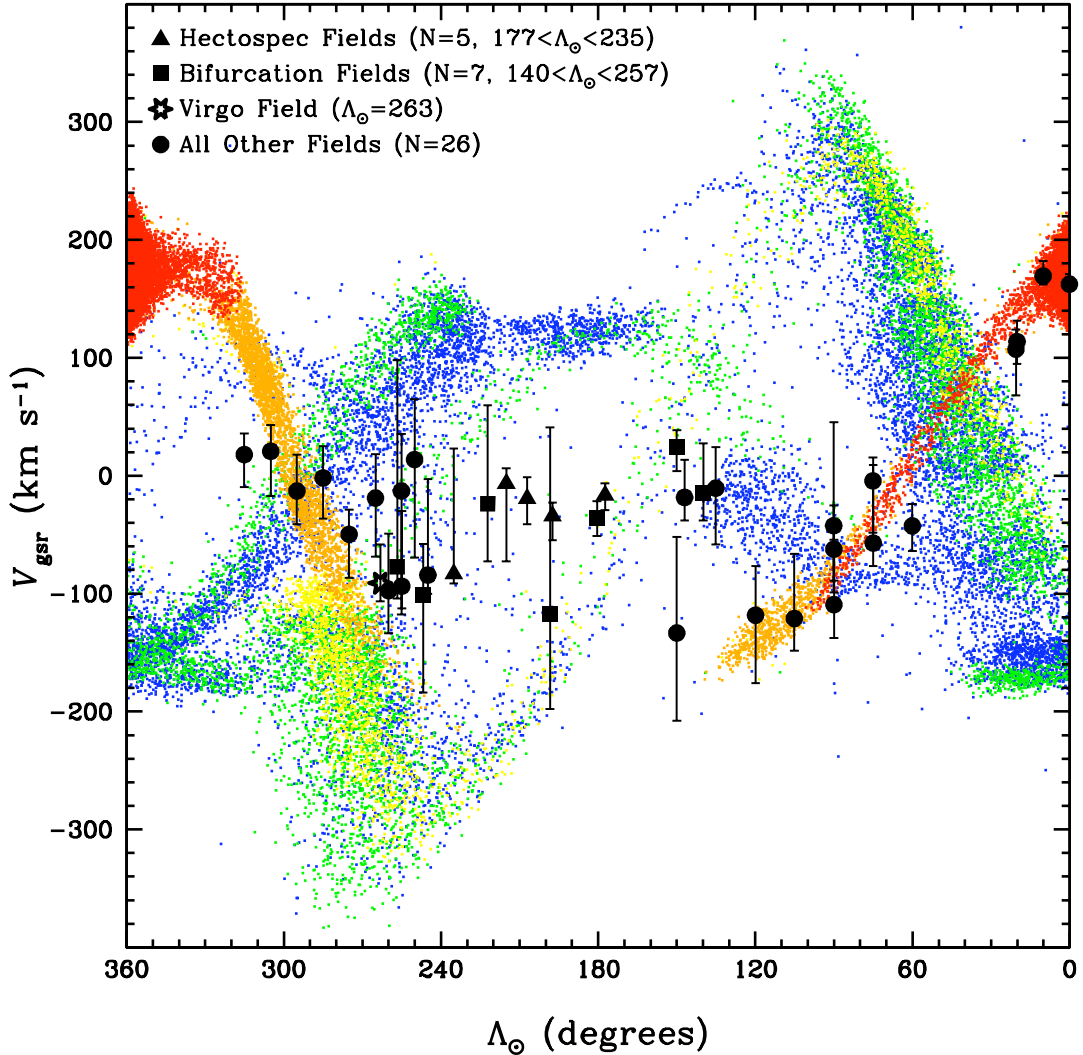
Figure 5.25: Comparison of spherical halo model and primary velocity peaks. The Galactic standard of rest radial velocities for the spherical halo model stars that satisfy the distance cut (described in Section 5.2.2.3) are shown as a function of their Sgr longitude. The model stars are color-coded as before to indicate on which orbit they became unbound from the core of Sgr. The black data points are plotted at the $(\Lambda_\odot, V_{\rm peak})$ values for the 39 fields in our survey. The five solid black triangles with $177° < \Lambda_\odot < 235°$ represent the Hectospec fields. The seven solid black squares with $140° < \Lambda_\odot < 257°$ represent the fields along the northern hemisphere bifurcation in the stream (Belokurov et al., 2006). The black star at $\Lambda_\odot = 263°$ denotes the Virgo field discussed in Chapter 4. The 26 solid black circles represent the remaining fields. Asymmetric error bars (as discussed in Section 5.1) are included for each observation. The peak velocities and the lengths of the error bars are listed for every field in Table 5.2.
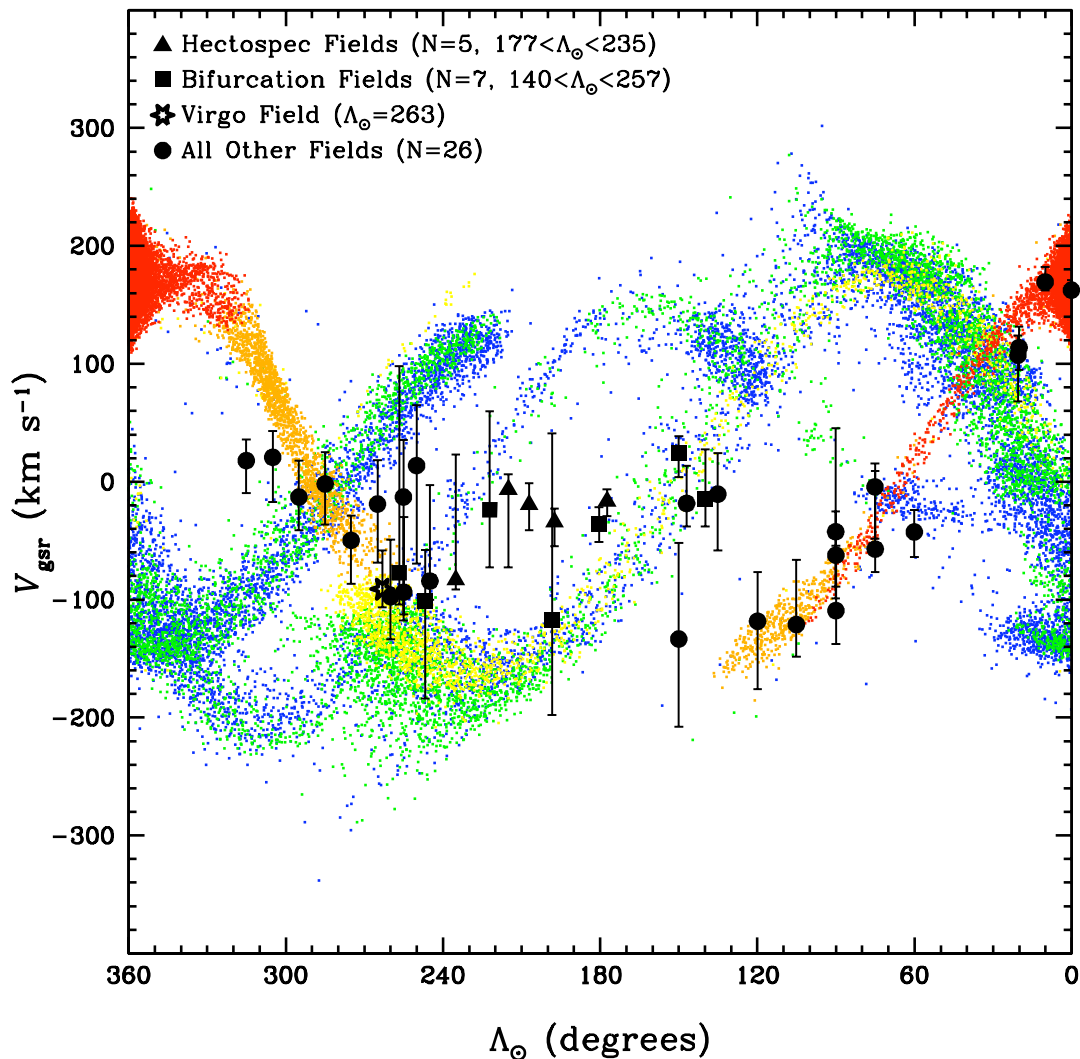
Figure 5.26: Comparison of prolate halo model and primary velocity peaks. The Galactic standard of rest radial velocities for the prolate halo model stars that satisfy the distance cut (described in Section 5.2.2.3) are shown as a function of their Sgr longitude. The model stars are color-coded as before to indicate on which orbit they became unbound from the core of Sgr. The black data points are plotted at the $(\Lambda_\odot, V_{peak})$ values for the 39 fields in our survey. The five solid black triangles with $177° < \Lambda_\odot < 235°$ represent the Hectospec fields. The seven solid black squares with $140° < \Lambda_\odot < 257°$ represent the fields along the northern hemisphere bifurcation in the stream (Belokurov et al., 2006). The black star at $\Lambda_\odot = 263°$ denotes the Virgo field discussed in Chapter 4. The 26 solid black circles represent the remaining fields. Asymmetric error bars (as discussed in Section 5.1) are included for each observation. The peak velocities and the lengths of the error bars are listed for every field in Table 5.2.
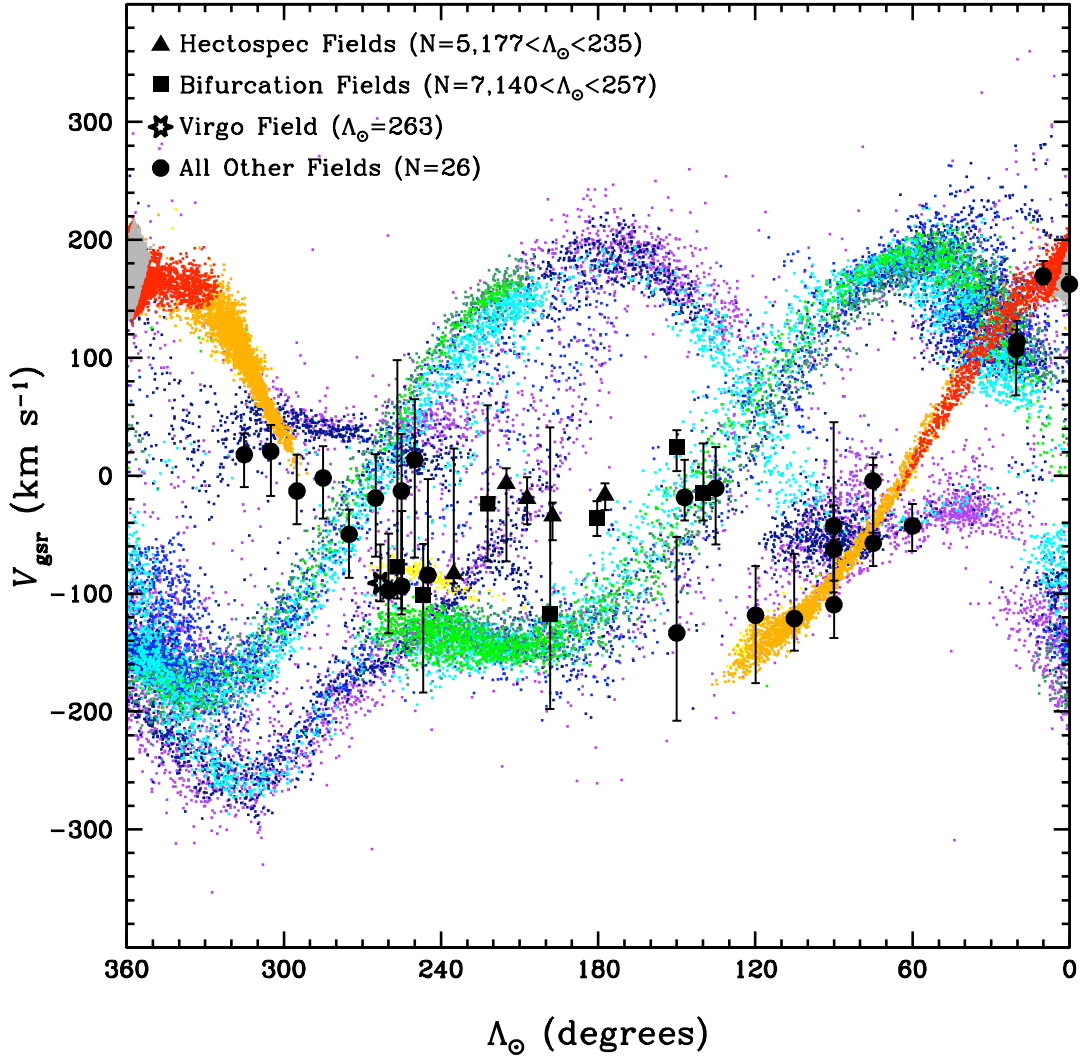
Figure 5.27: Comparison of triaxial halo model and primary velocity peaks. The Galactic standard of rest radial velocities for the triaxial halo model stars that satisfy the distance cut (described in Section 5.2.2.3) are shown as a function of their Sgr longitude. The model stars are color-coded as before to indicate on which orbit they became unbound from the core of Sgr. The black data points are plotted at the $(\Lambda_\odot, V_{peak})$ values for the 39 fields in our survey. The five solid black triangles with $177° < \Lambda_\odot < 235°$ represent the Hectospec fields. The seven solid black squares with $140° < \Lambda_\odot < 257°$ represent the fields along the northern hemisphere bifurcation in the stream (Belokurov et al., 2006). The black star at $\Lambda_\odot = 263°$ denotes the Virgo field discussed in Chapter 4. The 26 solid black circles represent the remaining fields. Asymmetric error bars (as discussed in Section 5.1) are included for each observation. The peak velocities and the lengths of the error bars are listed for every field in Table 5.2.

Figure 5.28: Comparisons of all four halo models and primary velocity peaks. The Galactic standard of rest radial velocities for stars that satisfy the distance cut (described in Section 5.2.2.3) in all four halo models are shown as a function of their Sgr longitude. The name of each model is centered near the top of its panel. The model stars are color-coded as before to indicate on which orbit they became unbound from the core of Sgr. The black data points are plotted at the $(\Lambda_\odot, V_{\mathrm{peak}})$ values for the 39 fields in our survey. The five solid black triangles with $177° < \Lambda_\odot < 235°$ represent the Hectospec fields. The seven solid black squares with $140° < \Lambda_\odot < 257°$ represent the fields along the northern hemisphere bifurcation in the stream (Belokurov et al., 2006). The black star at $\Lambda_\odot = 263°$ denotes the Virgo field discussed in Chapter 4. The 26 solid black circles represent the remaining fields. Asymmetric error bars (as discussed in Section 5.1) are included for each observation. The peak velocities and the lengths of the error bars are listed for every field in Table 5.2.
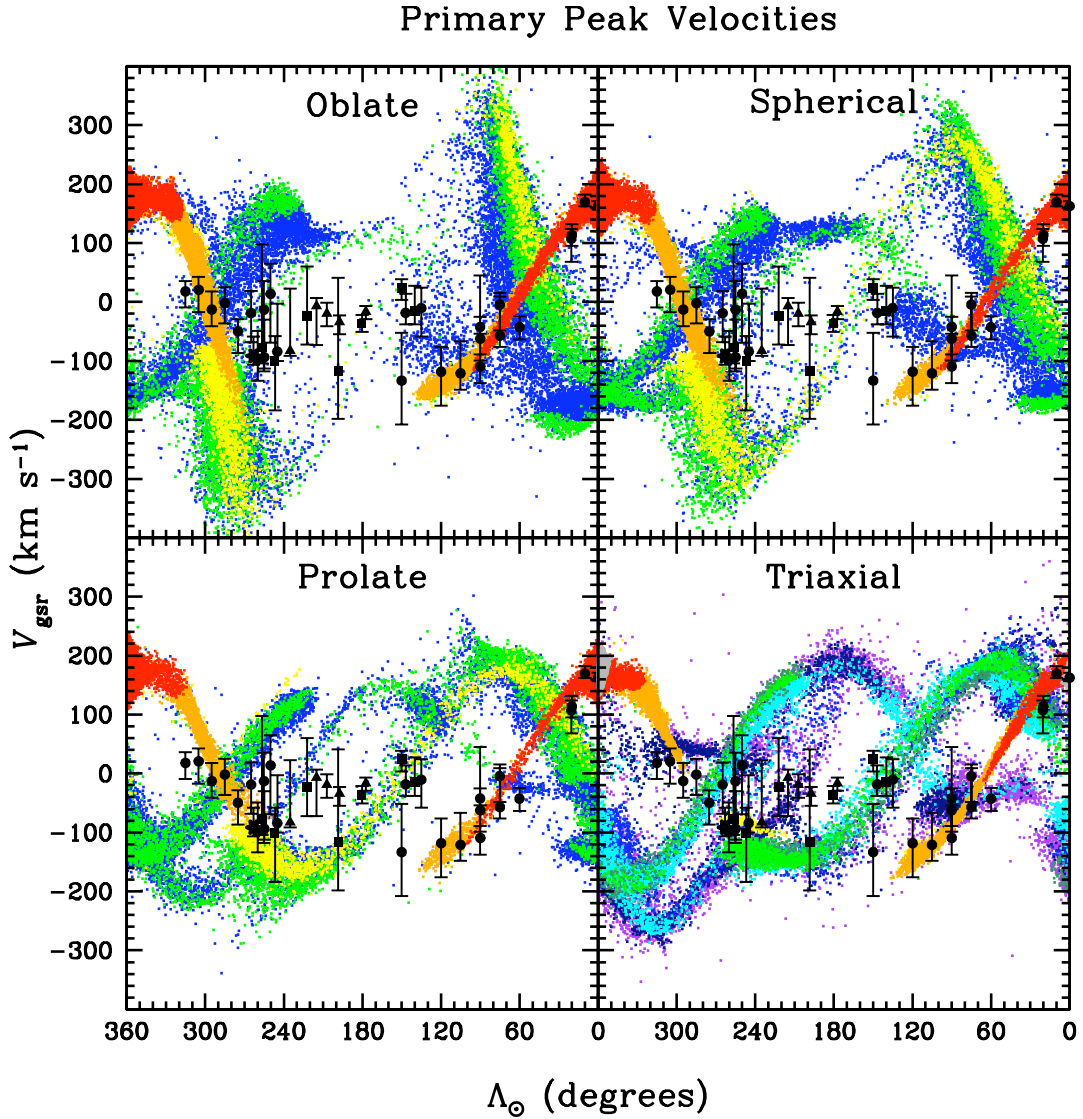
and the nearest field to it (at $\Lambda_\odot = 10°$, 169 km s^{-1}) agree with the predictions of the models of $\sim$170 km s^{-1}. This agreement is depicted graphically for the Sgr core in Figure 5.29, in which the peak velocities predicted by each of the models are seen to be in agreement with each other and with the observations.

Since the distance to the Sgr core is relatively well known, this field can provide insight on the accuracy of the photometric parallax technique (described in Section 5.2.2.2) used to estimate the distances of our survey stars. The upper panel of Figure 5.30 includes a distance histogram for all 372 observed stars in the Sgr core as well as a histogram for the 225-member subset with velocities consistent with the models' predictions for the core ($V_{\mathrm{gsr}} \simeq 170 \pm 50$ km s^{-1}). In the lower panels of Figure 5.30, histograms of the distances to the synthetic Sgr stars are shown for each of the four models. Note that the axisymmetric models of LJM05 assume the core of Sgr is at a distance of 24 kpc, while the triaxial model of LM10 assumes 28 kpc for its distance. Both of these values are within the 22–28 kpc range of published distance estimates for the Sgr core (summarized in Table 2 of Kunder & Chaboyer, 2009) derived from various observational studies. Since the distances of the model debris scale with the adopted value for the distance to the core, all of the debris in the triaxial model will be $\sim$17% further than if a distance of 24 kpc had been adopted, as was done for the axisymmetric models.

Although there is a predictably large spread in the distance estimates for the survey stars, the distribution peaks near 23 kpc, in good agreement with the previously mentioned studies. Of the subset of survey stars with velocities consistent with be-
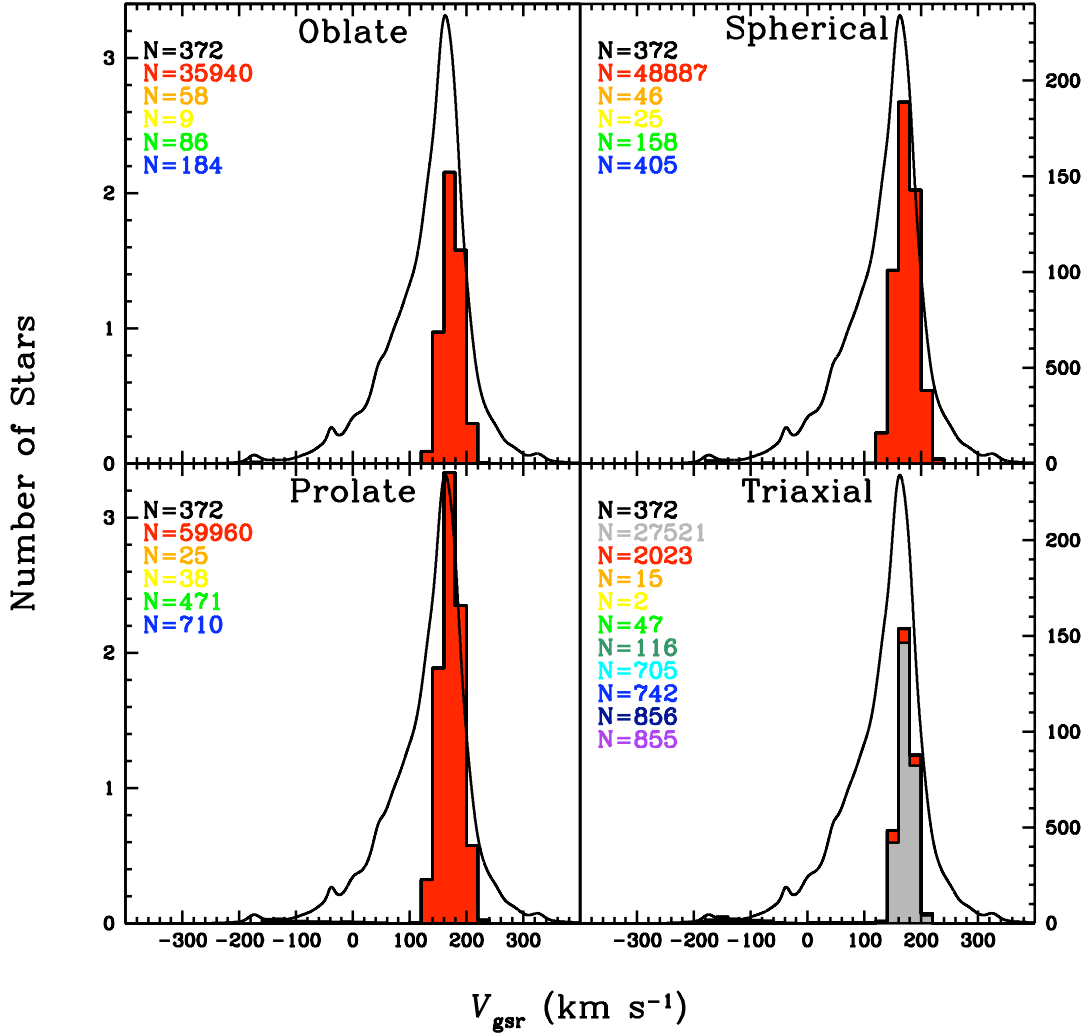
Figure 5.29: Velocity distributions of models and observations near $\Lambda_\odot = 0°$. Each of the four panels compares our observed velocity distribution in the $\Lambda_\odot = 0°$ field (black curve) to a histogram of the predicted velocities from either the oblate, spherical, prolate, or triaxial model. The model stars used for the comparisons were required to be within $10°$ of the center of the field and have distances that satisfy the cut described in Section 5.2.2.3 (i.e ≤ 50 kpc). The vertical scale on the left side of the figure applies to the observations, while the vertical scale on the right side of the figure applies to the models. The scale for the models was chosen (somewhat arbitrarily) so that the peak heights of the observed velocity distribution and the prolate model histogram appear equal. The model stars that comprise the histograms are color-coded (as before) to indicate the orbit on which they became unbound from the core. Their numbers are indicated in the upper left corner of each panel. As expected for this field, the vast majority of the selected model stars are still bound to the core. Distance histograms for this field are provided in Figure 5.30.
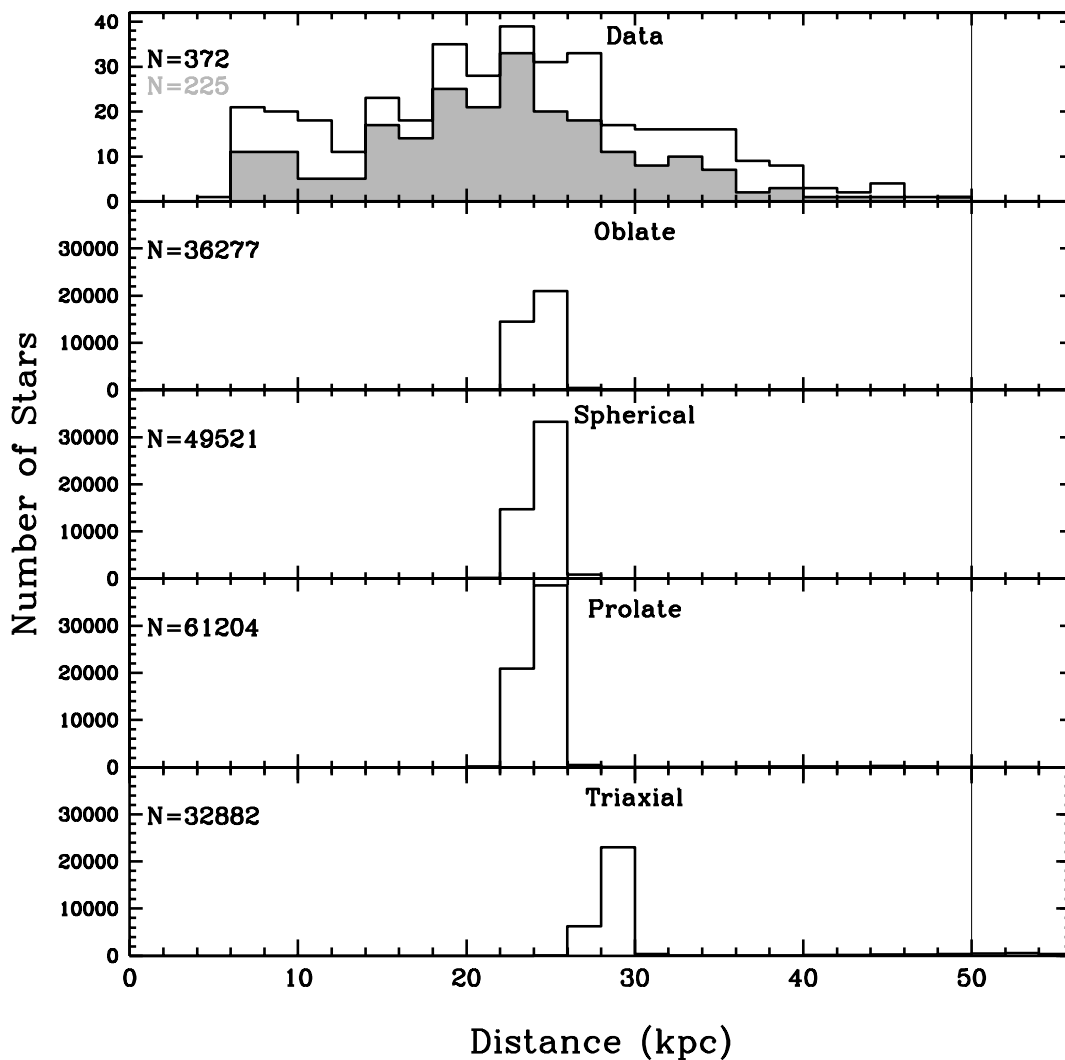
Figure 5.30: Distance histograms of models and observations near $\Lambda_\odot = 0°$. The upper panel shows the distance histograms for all 372 observed stars in the Sgr core as well as a histogram for the 225-member subset with velocities consistent with the models' predictions for the core ($V_{\rm gsr} \simeq 170\pm50$ km s^{-1}). The lower four panels show histograms of the distances of the oblate, spherical, prolate, or triaxial model stars within 10° of the center of our $\Lambda = 0°$ field. Note that the axisymmetric models of LJM05 assume the core of Sgr is at a distance of 24 kpc, while the triaxial model of LM10 assumes 28 kpc for its distance. The total number of stars in each distribution is indicated in the upper left corner of each panel. The vertical line at a distance of 50 kpc indicates the location of the distance cut (as described in Section 5.2.2.3) for this field. Velocity distributions for this field are provided in Figure 5.29.

longing to the core of Sgr ($V_{\mathrm{gsr}} \simeq 170 \pm 50$ km s^{-1}), 52% (117 of 225) have estimated distances in the range 23 ± 5 kpc. While the upper panel of Figure 5.30 illustrates the ability of our survey to effectively measure velocities for stars out to and beyond 40 kpc, it is important to remember that fainter, more distant stars were preferentially lost from our original selection of targets (see Section 3.3.4). This effect introduces an artificial bias in to the estimated distance distributions in our fields that can lead to slight underestimates of the distances to observed kinematic features.

A bit further out, at $\Lambda_\odot = 20°$, the peak velocities measured in the two fields there (114 and 107 km s^{-1}) reflect a slightly steeper velocity gradient relative to the core than that predicted by the models ($\sim$ –3 km s^{-1} deg^{-1}), but are consistent within the errors. All four models predict that the principle source of Sgr debris at this longitude should be due to young trailing stream stars with velocities of $\sim$150 km s^{-1}, as can be seen in Figure 5.28 (red points). This prediction is shown more clearly in Figure 5.31, in which the velocity distributions predicted by each of the models are compared with the combined velocity distribution for the two observed fields at $\Lambda_\odot = 20°$. In an effort to remove contamination from non-Sgr halo stars, a Gaussian distribution centered at 0 with a standard deviation of 100 km s^{-1} was subtracted from the observed distribution shown in all panels of Figure 5.31. The Gaussian was normalized to the equivalent of 19.4 stars, which ensured that the resulting distribution (after subtraction) had a minimum height of exactly zero.

Figure 5.31 reveals strong evidence in support of the triaxial model which is not immediately obvious upon first glance at Figure 5.28. In all four panels of Figure 5.31
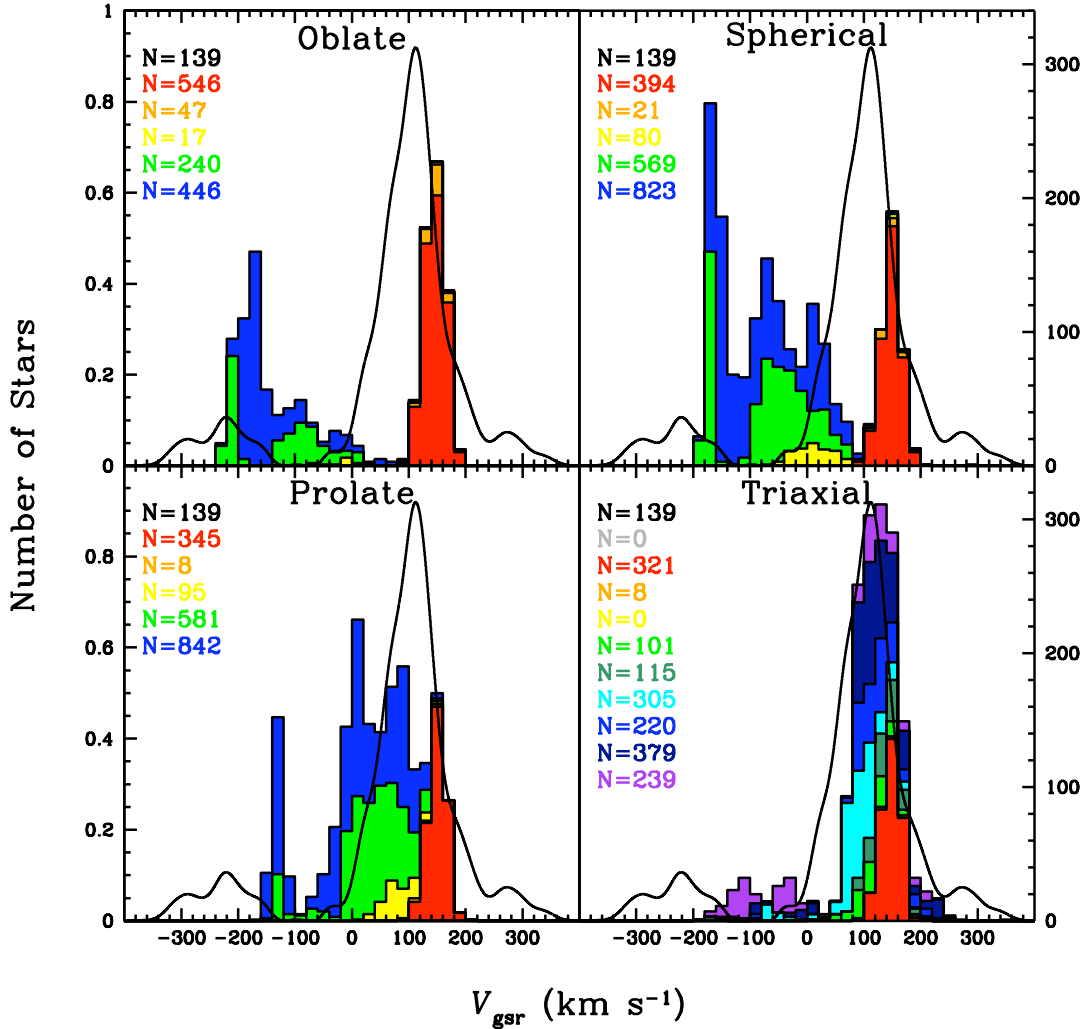
Figure 5.31: Velocity distributions of models and observations near $\Lambda_\odot = 20°$. Each of the four panels compares the combined velocity distribution from the two observed fields at $\Lambda_\odot = 20°$ (black curve) to a histogram of the predicted velocities from either the oblate, spherical, prolate, or triaxial model. The model stars used for the comparisons were required to be within 10° of the center of either field and have distances that satisfy the cut described in Section 5.2.2.3 (i.e ≤ 50 kpc). The vertical scale on the left side of the figure applies to the observations, while the vertical scale on the right side of the figure applies to the models. The scale for the models was chosen (somewhat arbitrarily) so that the peak heights of the observed velocity distribution and the triaxial model histogram appear equal. The model stars that comprise the histograms are color-coded (as before) to indicate the orbit on which they became unbound from the core. Their numbers are indicated in the upper left corner of each panel.

the young trailing model debris (red/orange) is consistently centered near 150 km s^{-1}, about 40 km s^{-1} higher than the observed peak. This is the immediate takeaway from inspection of Figure 5.28 near $\Lambda_\odot = 20°$. However, less obvious, is that in the progression of models from oblate, to spherical, to prolate, to triaxial, the velocities of the old leading stream debris (green/blue), 340° away from the core, move closer and closer to the expected trailing stream velocities. While this is depicted in Figure 5.28, Figure 5.31 makes these predictions much more apparent. In the case of the triaxial model only, the velocity distribution of the old leading stream debris is predicted to peak (at 120 km s^{-1}) near the observed peak. This feature makes the triaxial model a significantly superior match to the observations at this longitude[4].

It is worth emphasizing that while velocities from the dominant source of debris in this field (the young trailing stream) are incapable of discriminating between the various models, velocities from the secondary debris (due to the extension of the old leading stream) can very effectively discriminate between the models. The capability to detect the velocity signature from secondary debris at numerous fields along the Sgr stream is a powerful ability that is unique to this survey.

Further out, the peak velocities measured in the eight fields with $60° < \Lambda_\odot < 120°$ are seen to accurately trace the velocity trend predicted by the models (orange debris). Along this segment of the trailing stream the models all predict that the initially steep velocity gradient will ultimately flatten out to zero. This prediction is confirmed by our measurements. It is also possible that some of the very old (blue/purple) debris,

---

[4]A distance distribution for the fields at $\Lambda_\odot = 20°$ could not be generated because the photometry for the candidates in these fields could not be properly calibrated (see Section 2.3).

which is predicted to have similar velocities, may be somewhat blurring the signal from the young trailing stream, particularly in the $60° < \Lambda_\odot < 90°$ range.

Next along the trailing stream are five fields with $135° < \Lambda_\odot < 150°$. Four of these fields are clustered near -10 km s^{-1}, and the fifth field is offset to a highly negative radial velocity. That fifth field, which has very large error bars, and should thus be viewed with some skepticism, does not appear to match the predictions of any of the models. In all of the models, from $130° < \Lambda_\odot < 220°$ the young trailing stream debris lies beyond the observational limit of the survey (see Figure 5.23). This can be seen in Figures 5.24 to 5.28 where the young trailing stream (orange debris) abruptly vanishes near $(\Lambda_\odot, V_{\mathrm{gsr}}) \sim (130°, -120$ km s$^{-1})$, and then reappears (as green/blue debris) near $(220°, 160$ km s$^{-1})$. If the distance cut had not been applied, this measurement would have matched the trailing stream velocity trend predicted by all of the models (see Figure 5.16). If that particular data point is to be trusted, it would imply that some of the Sgr debris along the line of sight to that field may in fact be closer than the models suggests.

The other four fields in this area provide the first opportunity to discriminate between the various halo models. The observed velocities in these fields are not coincident with any identifiable debris in the oblate model. The spherical model predicts the presence of some old (blue) debris at similar velocities, but most of that debris seems to be just beyond the distance limit of these fields. The spherical model also predicts the presence of the extended leading stream (yellow/green debris) at very low density, but this is offset to somewhat higher velocities. In the prolate model,

however, the observed velocities of these four fields appear to be consistent, within the errors, with the extension of the leading stream (now considerably more dense than in the spherical model), $\sim215°$ away from the core. In the triaxial halo model, a similar, but even more robust correspondence is found between the observations in these four fields and the extended leading stream debris (green/dark green/cyan/blue), which is predicted to be at relatively high density here and to be a near perfect match to the measured velocities. The observations in this grouping of four fields can thus be interpreted to strongly favor the triaxial halo model. While the prolate model is also consistent with the observations, the spherical and (especially) the oblate models appear to be inconsistent with these observations. Note that as soon as the distance to the young trailing stream, which would otherwise be the dominant source of Sgr debris in these fields, exceeds the observation limits (near $\Lambda_\odot \sim130°$), the observed peak velocities suddenly shift to tracing the extended leading stream. This seems to reflect a general agreement between the models' predicted distances and the observational distance estimates (Section 5.2.2.2) for these fields.

Leading Stream

Now consider the leading stream of tidal debris. The peak velocity measurements for the first five fields along the young leading stream, with $275° < \Lambda_\odot < 315°$ (orange debris), follow the general trend of decreasing velocity as the angular separation from the core increases. The very first field, at $\Lambda_\odot = 315°$, underestimates the debris velocities in all four of the models. The next three fields, at $\Lambda_\odot = 305°$, $295°$, and $285°$, appear to be consistent, within the errors, with the results of the three axisymmetric

halo models. In the triaxial halo model, however, this segment of leading stream debris reaches distances that exceed the observational limit of the survey over the range $270° < \Lambda_\odot < 290°$. Therefore, the first two of these fields (at $\Lambda_\odot = 305°$ and $295°$) are consistent with the triaxial model's leading stream velocities, and the third field (at $\Lambda_\odot = 285°$) would be consistent as well if the distance cut had not been applied (see Figure 5.23). This implies that the Sgr debris along the line of sight to this particular field may in fact be a bit closer than the triaxial model suggests.

The fifth and final field in this group (at $\Lambda_\odot = 275°$) appears to be a useful discriminator between the various models. The observed peak velocity in that field (-50 km s^{-1}) is inconsistent with the oblate halo model, which predicts a highly negative velocity gradient along this portion of the young leading stream. It is consistent with the spherical halo model, within the errors, and is in excellent agreement with the prolate model. Leading stream debris in the triaxial halo model at the location of this particular field is still beyond the observational distance limit of the survey. Coincidentally, at $\Lambda_\odot = 275°$ the triaxial model predicts the young leading stream (if not removed by the distance cut) and the extended trailing stream (green/dark green/cyan) debris should have equal velocities of ~ -50 km s^{-1}, consistent with the observed value. The three axisymmetric models, however, predict the velocities of the extended trailing stream debris at this longitude to be significantly more positive. In summary, the peak velocity of this particular field is: (1) inconsistent with the oblate model; (2) consistent (within the errors) with leading stream debris in the spherical model; (3) consistent with leading stream debris in the triaxial model if the model

339

stars were a bit closer; and (4) most consistent with the predictions for leading stream debris in the prolate halo model or trailing stream debris in the triaxial model.

A bit further out along the young leading stream is a group of ten fields that span just 30° in longitude ($235° < \Lambda_\odot < 265°$). Seven of these fields have peak velocities in the range -101 km s^{-1} $< V_{\text{Peak}} < -77$ km s^{-1}, while the remaining three are offset to more positive velocities (-19, -13, and $+14$ km s^{-1}). The velocity measurements in those three fields are not compatible with any identifiable debris in the three axisymmetric models. They are, however, close to the expected velocities for the extended trailing stream in the triaxial model. But since two of these three fields contain a very low number of stars (6 and 16), this potential association should be considered questionable.

The other seven fields in this area, with a mean velocity of -90 km s^{-1}, provide the single strongest constraint on the halo's shape of the entire data set. These measurements clearly rule out the oblate and spherical models. In the prolate model, leading stream (yellow) debris has similar velocities, especially near $\Lambda_\odot = 260°$. However, the prolate model predicts a steep velocity gradient out to $\Lambda_\odot = 235°$ which is not seen in the data. The triaxial model provides the best match to these observations, particularly the younger (yellow) debris. Notably, the triaxial model is the only model to reproduce the nearly flat velocity gradient over this longitude range observed in the data.

Figure 5.32 compares the velocity distributions predicted by each of the four models with the combined velocity distribution from the 98 stars contained in three

selected fields (255.0n00.9, 256.7n04.1, 260.0p01.0) near $\Lambda_\odot = 257°$. In an effort to remove contamination from non-Sgr halo stars, a Gaussian distribution centered at 0 with a standard deviation of 100 km s^{-1} was subtracted from the observed distribution shown in all panels of Figure 5.32. The Gaussian was normalized to the equivalent of 31.7 stars, which ensured that the resulting distribution (after subtraction) had a minimum height of exactly zero.

The resulting observed velocity distribution has a prominent primary peak at –84 km s^{-1}, a secondary peak at 94 km s^{-1}, and a tertiary peak at 207 km s^{-1}. The velocity distributions predicted by each of the models feature a negative velocity peak due to young leading stream debris and a positive velocity peak due to older trailing stream debris. The locations, dispersions, and relative heights of these two features, however, differ from model to model. Figure 5.32 clearly illustrates the striking failure of the oblate and spherical models to reproduce the location and dispersion of the observed primary velocity feature. The prolate model, with a very similar dispersion, offers a much better match to the observed primary velocity feature, but the location of its peak is offset by about –45 km s^{-1} relative to the observed peak location. The triaxial model, when considering all model stars with distances $\leq$ 50 kpc, predicts a nearly perfect match to the location and dispersion of the observed primary velocity feature. When the distance cut (described in Section 5.2.2.3) is applied, eliminating model stars with distances beyond $\sim$39 kpc, the match is significantly worse. The location of the peak shifts by about –45 km s^{-1}, to the same value as predicted by the prolate model. This suggests that either (1) we systematically underestimated
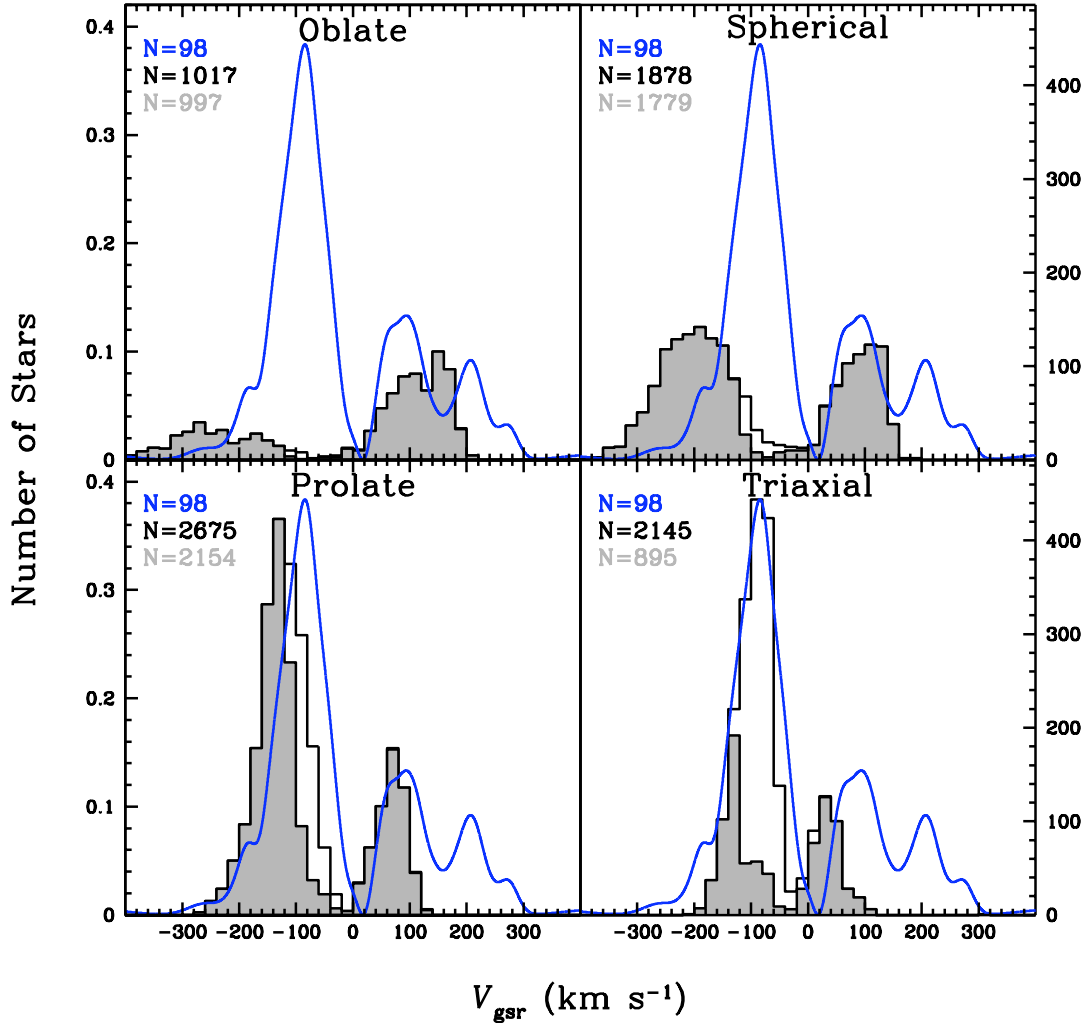
Figure 5.32: Velocity distributions of models and observations near $\Lambda_\odot = 257°$. Each of the four panels compares the combined velocity distribution from three observed fields (255.0n00.9, 256.7n04.1, 260.0p01.0) near $\Lambda_\odot = 257°$ (blue curve) to histograms of the predicted velocities from either the oblate, spherical, prolate, or triaxial model. All of the model stars used for the comparisons were required to be within $10°$ of the center of at least one of the three fields. The taller histograms in each panel include model stars with distances of ≤ 50 kpc, while the shorter histograms (shaded in grey) are a subset with distances that satisfy the cut described in Section 5.2.2.3 (i.e $\lesssim 39$ kpc). The vertical scale on the left side of the figure applies to the observations, while the scale on the right side of the figure applies to the models. The scale for the models was chosen (somewhat arbitrarily) so that the peak heights of the observed velocity distribution and the triaxial model histogram appear equal. The number of stars in each distribution are indicated in the upper left corner of each panel. Distance histograms for this field are provided in Figure 5.33.

the distances to the stars in these (and possibly all other) fields, (2) the distances predicted by the triaxial model to the majority of the stars in this kinematic feature have been overestimated, or (3) both (1) and (2) are true to some extent.

Comparisons between the models and the observations with respect to the secondary velocity feature, due to the old trailing debris, leads to a different set of conclusions. The spherical and prolate models are seen to match the location of the observed peak (94 km s^{-1}) the best. They are offset by just +15 km s^{-1} and -25 km s^{-1}, respectively. The oblate model continues to be a poor match to the observations, with a peak velocity offset of +55 km s^{-1} and a significantly larger dispersion than observed. The triaxial model, despite accurately predicting the location of the primary peak (when the relaxed distance cut is applied), is off by -65 km s^{-1} in its prediction for the location of the secondary peak.

It is also worth noting that the relative heights of the observed primary and secondary features are reproduced remarkably well by the prolate and triaxial (when the relaxed distance cut is applied) models. The oblate and spherical models, however, dramatically fail in this regard. While it is unclear to what extent the incompleteness of our survey in these fields affects this analysis, it is unlikely that correcting for the unknown incompleteness of the observations would significantly change the stated conclusions.

Overall the triaxial and prolate models provide the best matches to the locations of the observed primary and secondary velocity features, their relative heights, and their observed dispersions in these fields. This is only true for the triaxial model

343

if the relaxed distance cut ($<$50 kpc) is applied. While the prolate model is a bit off in its prediction for the location for the primary velocity peak (-45 km s^{-1}), the triaxial model is a bit off in its prediction for the location of the secondary velocity peak (-65 km s^{-1}). The predictions of the oblate and spherical models, however, are significantly worse in almost every regard. In short, the comparisons presented in Figure 5.32 strongly favor the triaxial and prolate models, and strongly disfavor the oblate and spherical models.

Our observations in these fields also detected a third kinematic feature consisting of 9 stars with highly positive radial velocities ($\sim$200 km s^{-1}). None of the models predict the existence of Sgr debris with such high velocities in these fields. It is therefore likely that this feature represents the detection of a comoving group of stars in the Galactic halo that is unrelated to Sgr, but may possibly be associated with a previously discovered or as yet unknown tidal stream.

The top panel of Figure 5.33 presents the distance histograms for the observed primary (blue), secondary (red), and tertiary (green) velocity features. The lower four panels show the distance histograms for the primary (blue) and secondary (red) features as predicted by each of the four models. The observed kinematic features are not neatly separated from one another in distance. Instead, they are seen to overlap each other, as all of the models predict. The estimated distances to the observed stars, however, are significantly smaller than the models predict. This is especially true for the triaxial and (to a lesser extent) the prolate models, which predict a significant fraction of the primary feature stars beyond the $\sim$39 kpc observational limit for these

344

fields. This figure more clearly illustrates a important point made earlier. Given that the location of the primary velocity peak is so well matched by the predictions of the triaxial and prolate models, especially the model stars beyond the nominal 39 kpc limit, it is highly likely that either the distances to the observed stars have been systematically underestimated, the distances predicted by the triaxial and prolate models to these stars have been overestimated, or both.

Next along the stream, are five fields that span 25° of longitude from $197° < \Lambda_\odot < 222°$. One of these fields, with a peak velocity of –117 km s^{-1}, appears consistent with the predictions for leading stream (yellow/green) debris in the prolate and triaxial models. However, since this field only contains velocities for six stars, and the error bars on its peak velocity are quite large, it is probably best to disregard it.

The other four fields in this area, with a mean velocity of –21 km s^{-1}, do not seem to match any identifiable debris in the three axisymmetric models. In the triaxial halo model there is some very old (navy blue/purple) trailing stream debris at similar velocities, but predictions for debris this old (>6 Gyr and ∼570° in angular separation from the core) are highly unlikely to be accurate. It then becomes difficult to explain the lack of a detection of Sgr in these fields. The prolate and triaxial models predict a significant amount of leading stream (yellow/green) debris with highly negative radial velocities (∼–150 km s^{-1}). The triaxial model also predicts the presence of some older trailing stream (green/dark green/cyan) debris with velocities of ∼150 km s^{-1}. But neither of these was detected. We note that three of these fields are located on the low-density branch of the northern hemisphere bifurcation, and that their spectroscopy
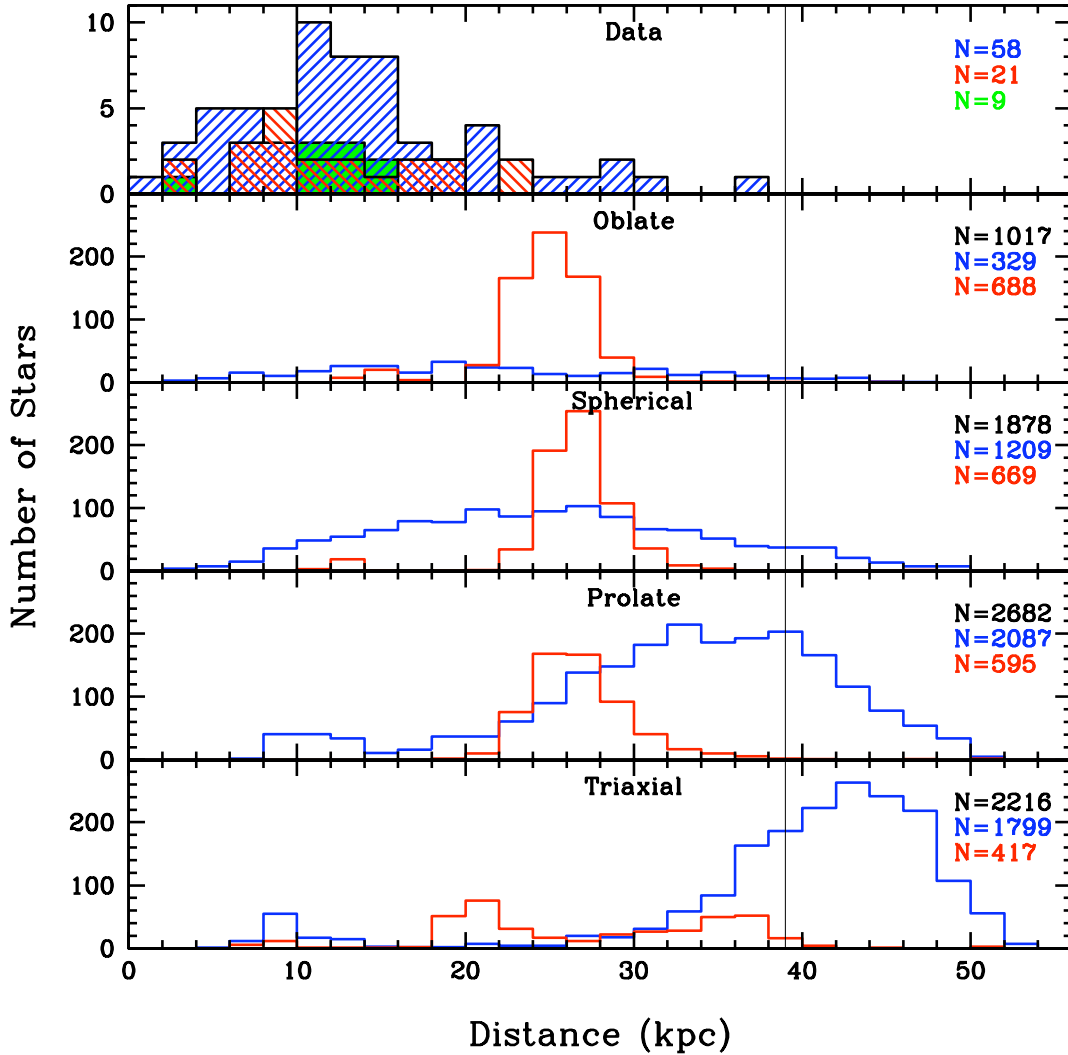
345

Figure 5.33: Distance histograms of models and observations near $\Lambda_\odot = 257°$. The upper panel shows the distance histograms for three subsets of the 98 observed stars from the three combined fields (255.0n00.9, 256.7n04.1, 260.0p01.0) near $\Lambda_\odot = 257°$. The blue histogram includes the 58 stars in the primary velocity peak of Figure 5.32 with -200 km s^{-1} < $V_{\rm gsr}$ < 20 km s^{-1}. The red histogram includes the 21 stars in the secondary velocity peak with 20 km s^{-1} < $V_{\rm gsr}$ < 160 km s^{-1}. The green histogram includes the 9 stars in the tertiary velocity peak with 160 km s^{-1} < $V_{\rm gsr}$ < 250 km s^{-1}. The blue/red histograms in the lower four panels show the distance distributions for the primary/secondary velocity peak in the model distributions (shown in Figure 5.32) consisting of stars that are within 10° of the center of at least one of the three observed fields and have velocities that are less/greater than -20 km s^{-1}. The total number of stars in each distribution is indicated in the upper right corner of each panel. The vertical line at a distance of 39 kpc indicates the location of the distance cut (described in Section 5.2.2.3) for this field.

was acquired with Hectospec. Candidate selection for the Hectospec fields did not go as deep as for the IMACS fields (compare the upper right panels of Figures 3.36 and 3.37). Thus, it may be that the lack of a detection in these fields is due to the combination of two factors: (1) the expectedly low density of Sgr debris in these fields (Belokurov et al., 2006, see their Figure 1), and (2) the failure to select candidate stars at the appropriate distance.

Finally, there are two fields located near $\Lambda_{\odot}{\sim}180°$ with peak velocities of –17 and –36 km s^{-1} that do not appear to coincide with Sgr debris in any of the models. The models' predictions for leading stream debris come the closest, but are offset to significantly lower velocities ($\sim$–100 km s^{-1}) at this longitude. Given the proximity of the measured velocities to zero, it is possible that the majority of the observed stars are unassociated with Sgr and are in fact members of the smooth stellar halo or the thick disk. In fact, these two fields are at the lowest galactic latitudes ($b \sim 11°$) of any fields in the survey. It is also worth noting that the spectroscopy in one of these fields was acquired with Hectospec, so it may have suffered from the same issues mentioned above.

5.2.3.2 Secondary Velocity Peaks

In Section 5.1, in addition to identifying the primary velocity peak in each field's velocity distribution profile, secondary velocity peaks were also identified (see Figures 5.3 to 5.12 and Table 5.2). It may be that some of these secondary velocity peaks represent identifications of additional Sgr debris in these fields. To test this hypothesis

we compare the secondary velocity peaks from our survey with predictions from the models of LJM05 and LM10.

In Figures 5.34 to 5.37 the Galactic standard of rest radial velocities of the model stars are plotted as a function of their Sgr longitude, $\Lambda_\odot$, for the oblate, spherical, prolate, and triaxial models, respectively. Only model stars that satisfy the distance cut introduced in Section 5.2.2.3 are included[5]. The model stars are color-coded in accordance with the system adopted in Section 5.2.1, which uses the orbit on which the particles became unbound from the core as an indicator of their dynamical age. Overplotted in each of these figures are the 30 secondary velocity peaks originally identified in Section 5.1. The 39 primary velocity peaks are also shown with open symbols for reference. The peak velocities and the sizes of the asymmetric error bars are listed for every field in Table 5.2. To make visual comparisons between the different models easier, Figure 5.38 combines Figures 5.34 to 5.37 in to a single figure.

It is likely that in numerous cases the secondary velocity peaks do not correspond to identifiable Sgr debris. They may be the signatures of other kinematic features in the halo, or, perhaps more likely, just "noise" in the velocity distribution profiles. The best evidence that the secondary velocity peaks are in fact associated with Sgr can be provided by neighboring fields that trace a continuous velocity trend over a range of longitudes.

---

[5]Plots of V_{gsr} as a function of $\Lambda_\odot$ that include all 10^5 model stars were presented in Figure 5.16.
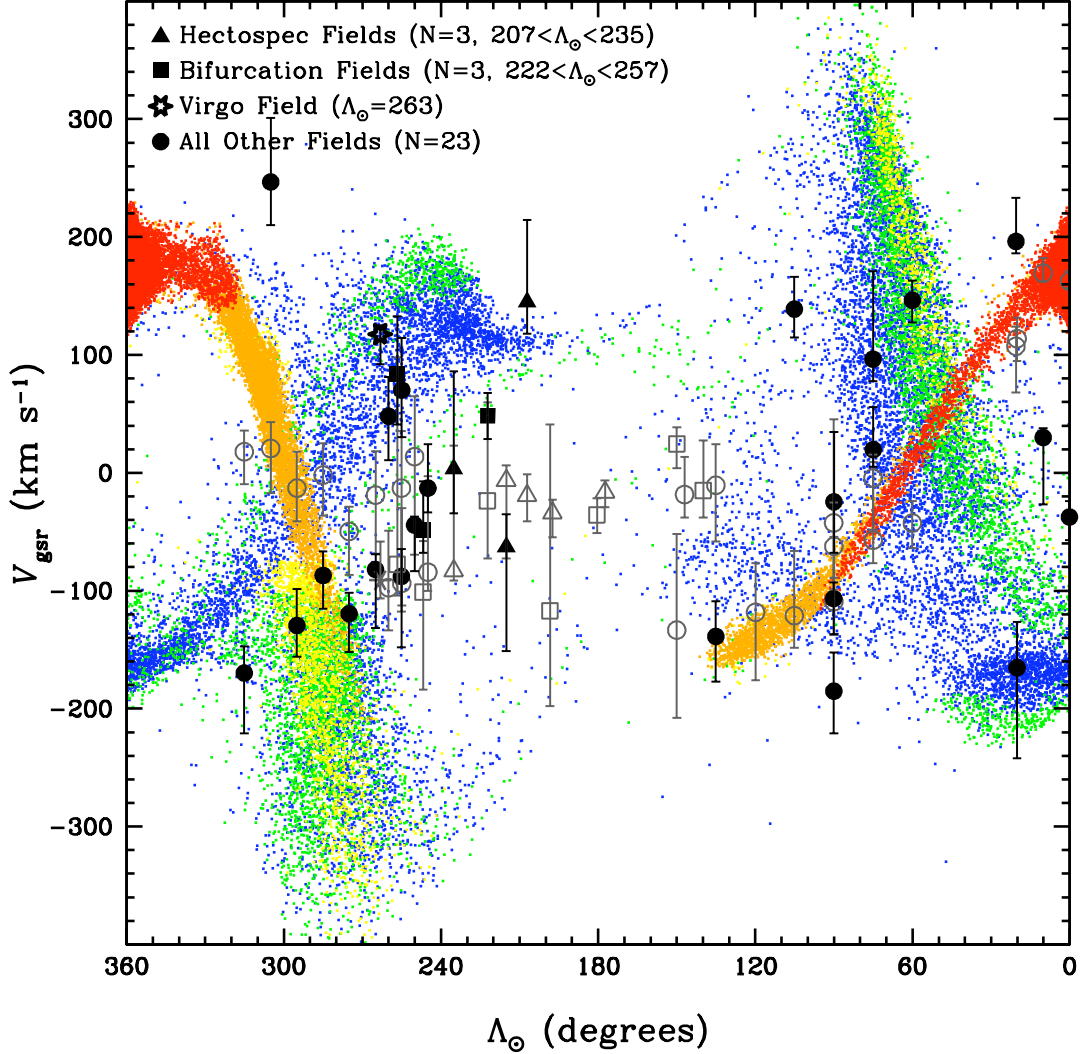
Figure 5.34: Comparison of oblate halo model and secondary velocity peaks. The Galactic standard of rest radial velocities for the oblate halo model stars that satisfy the distance cut (described in Section 5.2.2.3) are shown as a function of their Sgr longitude. The model stars are color-coded as before to indicate on which orbit they became unbound from the core of Sgr. The black data points are plotted at the $(\Lambda_{\odot}, V_{peak2})$ values for the 30 fields in our survey that contain an identified secondary velocity peak. The three solid black triangles with $207° < \Lambda_{\odot} < 235°$ represent the Hectospec fields. The three solid black squares with $222° < \Lambda_{\odot} < 257°$ represent the fields along the northern hemisphere bifurcation in the stream (Belokurov et al., 2006). The black star at $\Lambda_{\odot} = 263°$ denotes the Virgo field discussed in Chapter 4. The 23 solid black circles represent the remaining fields. Asymmetric error bars (as discussed in Section 5.1) are included for each observation. The grey open symbols represent the primary velocity peaks plotted in Figures 5.24 to 5.28. The peak velocities and the lengths of the error bars are listed for every field in Table 5.2.
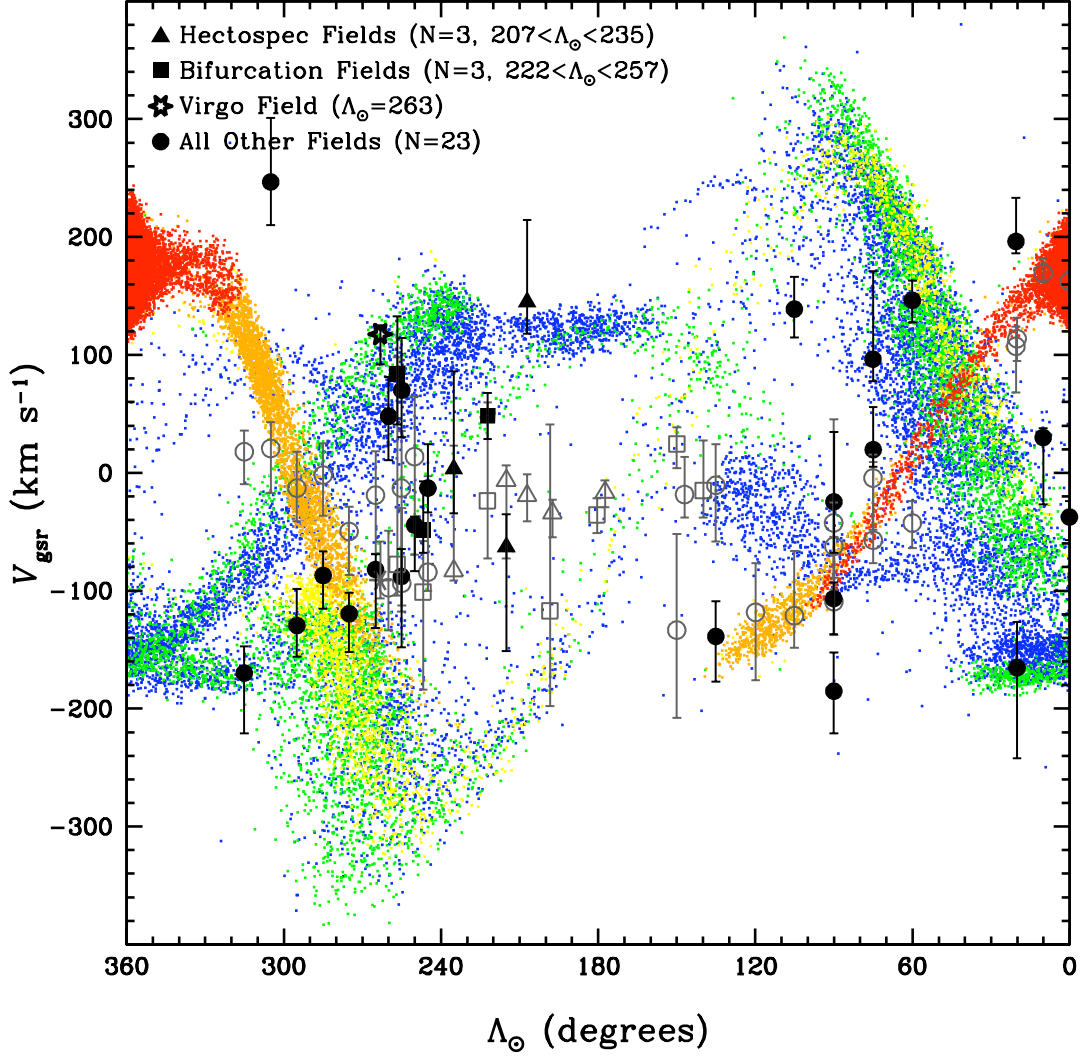
Figure 5.35: Comparison of spherical halo model and secondary velocity peaks. The Galactic standard of rest radial velocities for the spherical halo model stars that satisfy the distance cut (described in Section 5.2.2.3) are shown as a function of their Sgr longitude. The model stars are color-coded as before to indicate on which orbit they became unbound from the core of Sgr. The black data points are plotted at the $(\Lambda_\odot, V_{peak2})$ values for the 30 fields in our survey that contain an identified secondary velocity peak. The three solid black triangles with $207° < \Lambda_\odot < 235°$ represent the Hectospec fields. The three solid black squares with $222° < \Lambda_\odot < 257°$ represent the fields along the northern hemisphere bifurcation in the stream (Belokurov et al., 2006). The black star at $\Lambda_\odot = 263°$ denotes the Virgo field discussed in Chapter 4. The 23 solid black circles represent the remaining fields. Asymmetric error bars (as discussed in Section 5.1) are included for each observation. The grey open symbols represent the primary velocity peaks plotted in Figures 5.24 to 5.28. The peak velocities and the lengths of the error bars are listed for every field in Table 5.2.
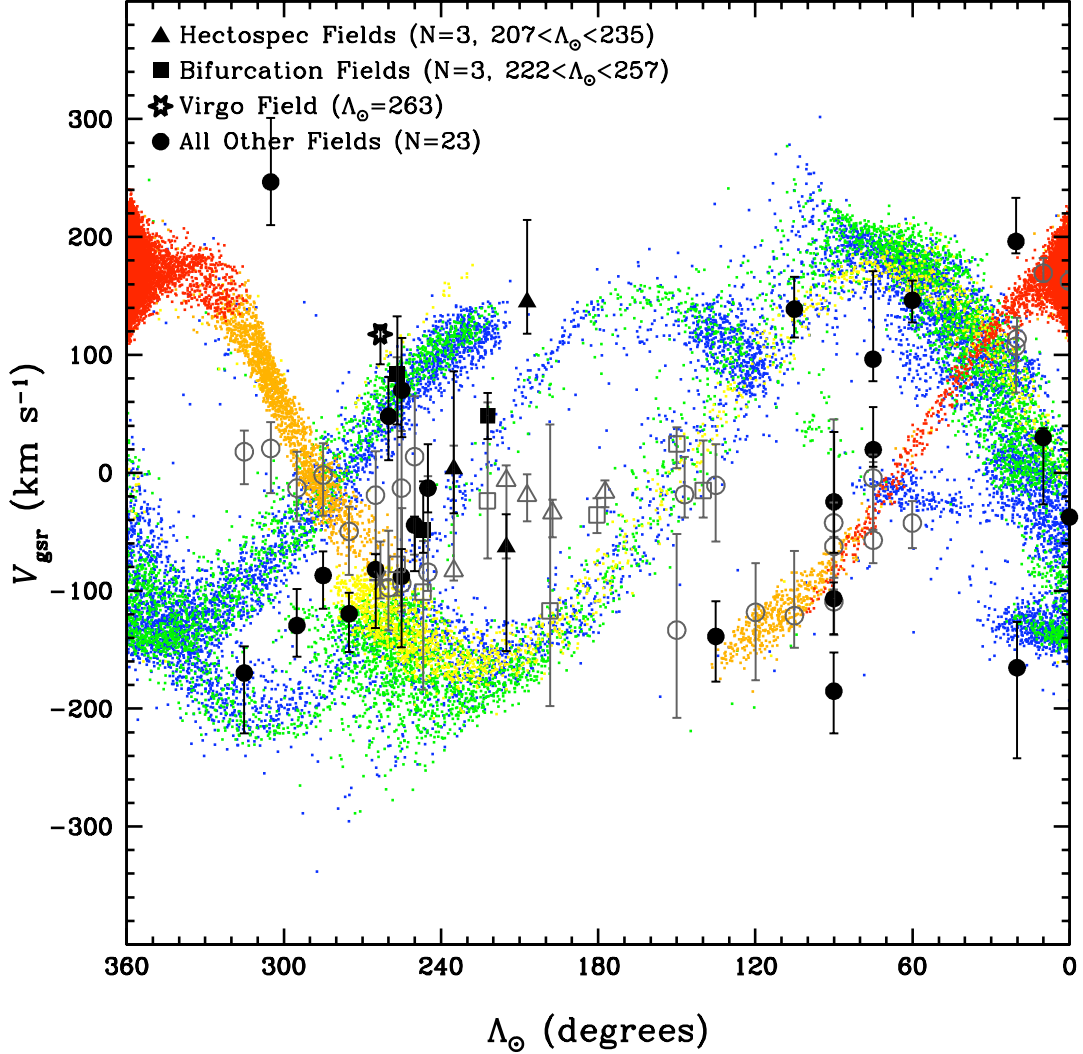
Figure 5.36: Comparison of prolate halo model and secondary velocity peaks. The Galactic standard of rest radial velocities for the prolate halo model stars that satisfy the distance cut (described in Section 5.2.2.3) are shown as a function of their Sgr longitude. The model stars are color-coded as before to indicate on which orbit they became unbound from the core of Sgr. The black data points are plotted at the $(\Lambda_\odot, V_{peak2})$ values for the 30 fields in our survey that contain an identified secondary velocity peak. The three solid black triangles with $207° < \Lambda_\odot < 235°$ represent the Hectospec fields. The three solid black squares with $222° < \Lambda_\odot < 257°$ represent the fields along the northern hemisphere bifurcation in the stream (Belokurov et al., 2006). The black star at $\Lambda_\odot = 263°$ denotes the Virgo field discussed in Chapter 4. The 23 solid black circles represent the remaining fields. Asymmetric error bars (as discussed in Section 5.1) are included for each observation. The grey open symbols represent the primary velocity peaks plotted in Figures 5.24 to 5.28. The peak velocities and the lengths of the error bars are listed for every field in Table 5.2.

Figure 5.37: Comparison of triaxial halo model and secondary velocity peaks. The Galactic standard of rest radial velocities for the triaxial halo model stars that satisfy the distance cut (described in Section 5.2.2.3) are shown as a function of their Sgr longitude. The model stars are color-coded as before to indicate on which orbit they became unbound from the core of Sgr. The black data points are plotted at the $(\Lambda_\odot, V_{peak2})$ values for the 30 fields in our survey that contain an identified secondary velocity peak. The three solid black triangles with $207° < \Lambda_\odot < 235°$ represent the Hectospec fields. The three solid black squares with $222° < \Lambda_\odot < 257°$ represent the fields along the northern hemisphere bifurcation in the stream (Belokurov et al., 2006). The black star at $\Lambda_\odot = 263°$ denotes the Virgo field discussed in Chapter 4. The 23 solid black circles represent the remaining fields. Asymmetric error bars (as discussed in Section 5.1) are included for each observation. The grey open symbols represent the primary velocity peaks plotted in Figures 5.24 to 5.28. The peak velocities and the lengths of the error bars are listed for every field in Table 5.2.
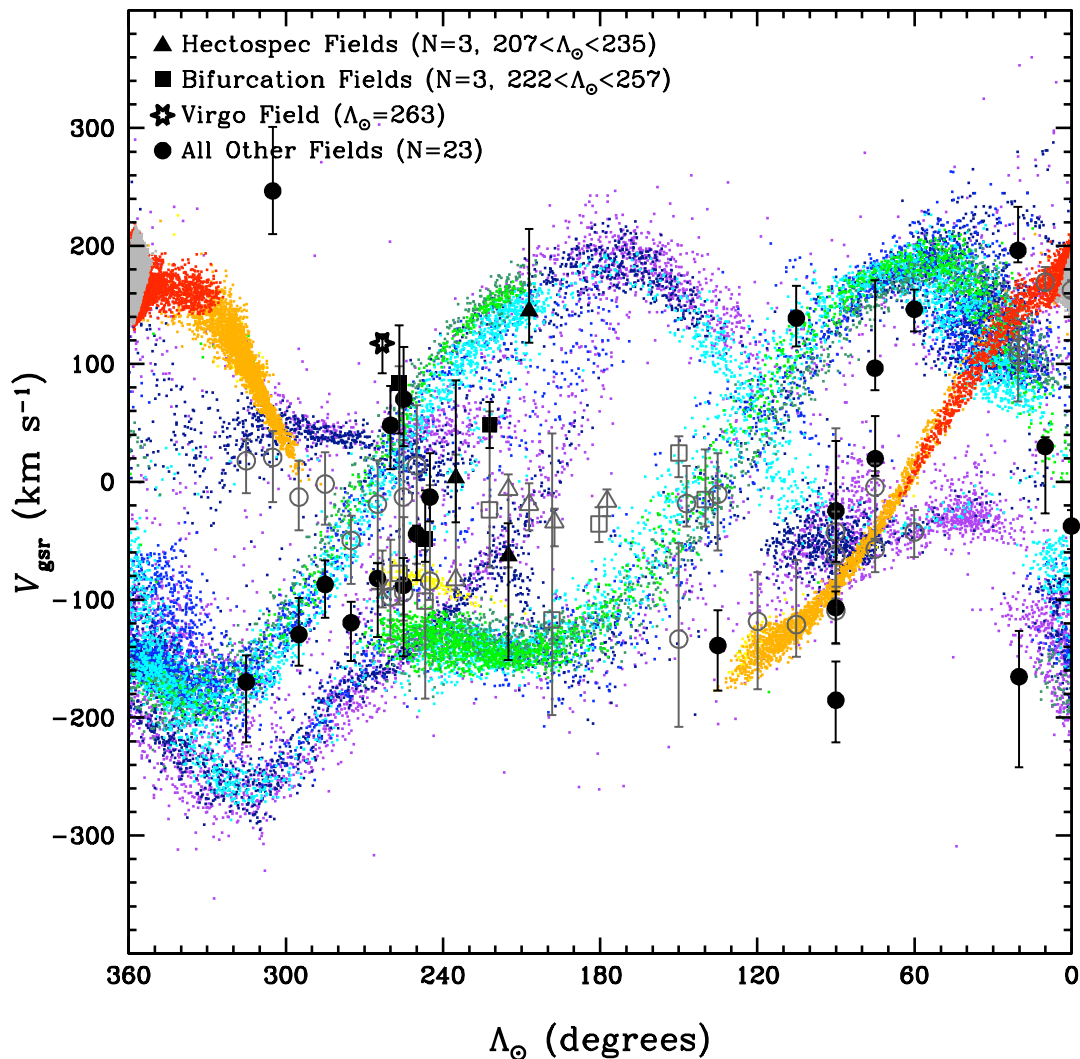
Figure 5.38: Comparisons of all four halo models and secondary velocity peaks. The Galactic standard of rest radial velocities for stars that satisfy the distance cut (described in Section 5.2.2.3) in all four halo models are shown as a function of their Sgr longitude. The name of each model is centered near the top of its panel. The model stars are color-coded as before to indicate on which orbit they became unbound from the core of Sgr. The black data points are plotted at the $(\Lambda_\odot, V_{peak2})$ values for the 30 fields in our survey that contain an identified secondary velocity peak. The three solid black triangles with $207° < \Lambda_\odot < 235°$ represent the Hectospec fields. The three solid black squares with $222° < \Lambda_\odot < 257°$ represent the fields along the northern hemisphere bifurcation in the stream (Belokurov et al., 2006). The black star at $\Lambda_\odot = 263°$ denotes the Virgo field discussed in Chapter 4. The 23 solid black circles represent the remaining fields. Asymmetric error bars (as discussed in Section 5.1) are included for each observation. The peak velocities and the lengths of the error bars are listed for every field in Table 5.2. Symbols used to represent the primary velocity peaks in Figures 5.34 to 5.37 have been excluded for clarity.

Leading Stream

In the area where the dominant source of Sgr debris is expected to be associated with the young trailing stream ($0° < \Lambda_\odot < 135°$), the source of the secondary velocity peaks is expected to be the extended leading stream. There are twelve fields with identified secondary velocity peaks in this area. While a few of the measured velocities are consistent with the predictions of the various models, in general, they do not appear to continuously trace any of the expected velocity trends for Sgr debris at these longitudes. There are five measurements that are consistent with the prolate and triaxial models' predictions for the extended leading stream (yellow/green/dark green) debris, but the lack of a detection in the other seven fields raises doubts.

Trailing Stream

The results in the area of the young leading stream ($207° < \Lambda_\odot < 315°$) are much more intriguing. In this area the source of the secondary velocity peaks is expected to be the extended trailing stream. First consider the three fields with highly negative radial velocities and $285° < \Lambda_\odot < 315°$. These could be interpreted as detections of the young leading stream in the oblate or spherical models. But it is expected that the leading stream debris should correspond to the primary velocity peaks at these longitudes, not the secondary peaks. The velocities in these three fields fall right between the predictions for the extended trailing stream and the old leading stream in the prolate halo model. However, they are seen to perfectly trace the velocity trend along the extended trailing debris stream (green/cyan particles) in the triaxial halo model.

Furthermore, there are an additional three fields with positive velocities clustered near $\Lambda_\odot \sim 255°$. These measurements are fairly well matched by the predicted velocities for the extended trailing stream in all four of the models. A deeper discussion and analysis of the secondary velocity peaks in these three fields was provided earlier along with the presentation of Figures 5.32 and 5.33.

A bit further out, at $\Lambda_\odot = 207°$, is a single field with a highly positive radial velocity ($\sim$145 km s^{-1}). This measurement is also consistent with predictions for the extended trailing stream (cyan debris) by the triaxial model. In the three axisymmetric models, however, the distance cut has removed most of the trailing stream debris at this longitude.

Finally, there is a well defined velocity trend across eight fields from $(\Lambda_\odot, V_{\mathrm{gsr}}) = (275°,-120$ km s$^{-1})$ to $(222°,49$ km s$^{-1})$. No debris in the oblate and spherical models appears to match this trend. In the triaxial model, the young leading stream (yellow/green debris) is well matched to the subset of these that are at higher longitudes, but the remaining measurements do not appear to be consistent with any Sgr debris. In the prolate model, however, those five remaining velocity measurements trace the velocity trend of the old leading stream (green/blue debris), more than 360° in angular separation from the core. This may just be a coincidence, as the dominant source of the secondary velocity peaks at these longitudes ($222° < \Lambda_\odot < 250°$) is expected to be the from extended trailing stream.

5.2.3.3 Disentangling the Triaxial Model Results

One major difference between the axisymmetric models of LJM05 and the triaxial model of LM10 was the total time over which the simulations were integrated (4.0 Gyr versus 7.8 Gyr, respectively). To help see the effects of this more clearly Figures 5.39 (for primary velocity peaks) and 5.40 (for secondary velocity peaks) are included. Both of these figures plot the Galactic standard of rest radial velocities as a function of their Sgr longitude, $\Lambda_\odot$, for the triaxial model stars that satisfy the applied distance cut (Section 5.2.2.3). The four panels in each of these figures sequentially exclude the debris lost during the single oldest orbit remaining in the previous panel. The final panels (bottom right) only include debris lost over the last four complete orbits (4.2 Gyr), similar to the axisymmetric models.

Since all of the particles in the triaxial model are tagged as belonging to either the leading or trailing stream, this information can be used to disentangle their overlapping radial velocity trends. Figure 5.41 plots the Galactic standard of rest radial velocities as a function of their Sgr longitude, $\Lambda_\odot$, for the triaxial model stars that satisfy the applied distance cut (Section 5.2.2.3). The left and right panels exclusively show the leading and trailing stream debris, respectively. In the upper and lower panels the primary and secondary velocity peaks are overplotted, respectively. This figure can be used to easily identify which stream is the source of Sgr debris in regions where they overlap, and it was particularly helpful with the analysis presented earlier in this section.

356

Figure 5.39: Age-limited triaxial halo model and primary velocity peaks. The Galactic standard of rest radial velocities for the triaxial halo model stars that satisfy the distance cut (described in Section 5.2.2.3) are shown as a function of their Sgr longitude. The four panels sequentially exclude the debris lost during the single oldest orbit remaining in the previous panel. Specifically, the upper left panel excludes the oldest (6.9–7.8 Gyr) debris from the eighth (purple) orbit that has been included in all previous triaxial halo model plots. The upper right panel additionally excludes debris lost 6.0–6.9 Gyr ago during the seventh (navy blue) orbit. The lower left panel additionally excludes debris lost 5.1–6.0 Gyr ago during the sixth (blue) orbit. Finally, the lower right panel additionally excludes debris lost 4.2–5.0 Gyr ago during the fifth (cyan) orbit. This panel includes currently bound stars (grey), debris lost over the current orbit (red, 0–0.5 Gyr), and the four previous orbits (orange, 0.5–1.3 Gyr; yellow, 1.4–2.3 Gyr; green, 2.4–3.2 Gyr; and dark green, 3.2–4.2 Gyr). The range of included orbits are listed near the top of each panel. The black data points with asymmetric error bars are plotted at the $(\Lambda_\odot, V_{peak})$ values (see Table 5.2) for the 39 fields in our survey using the same symbols as in the previous primary velocity peak plots.
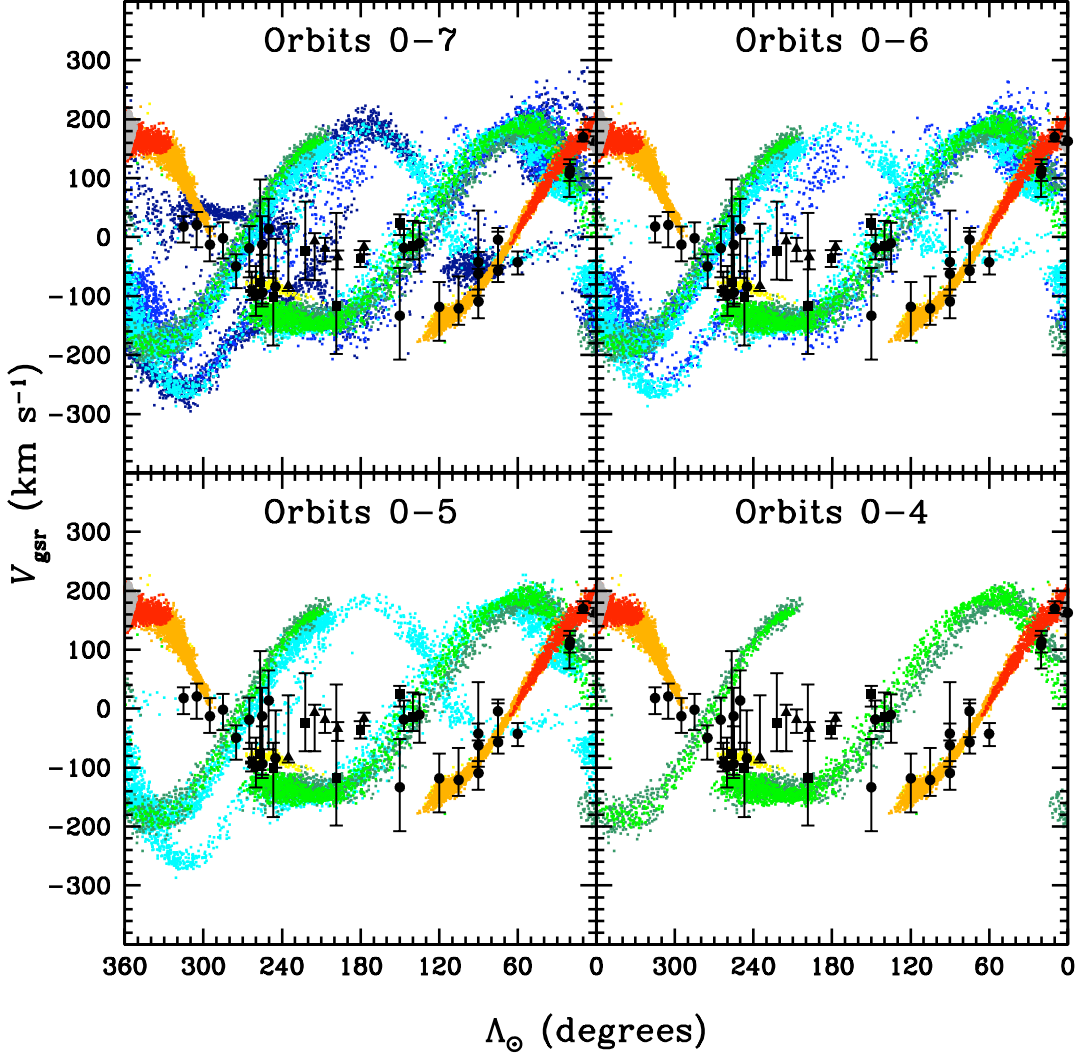
357
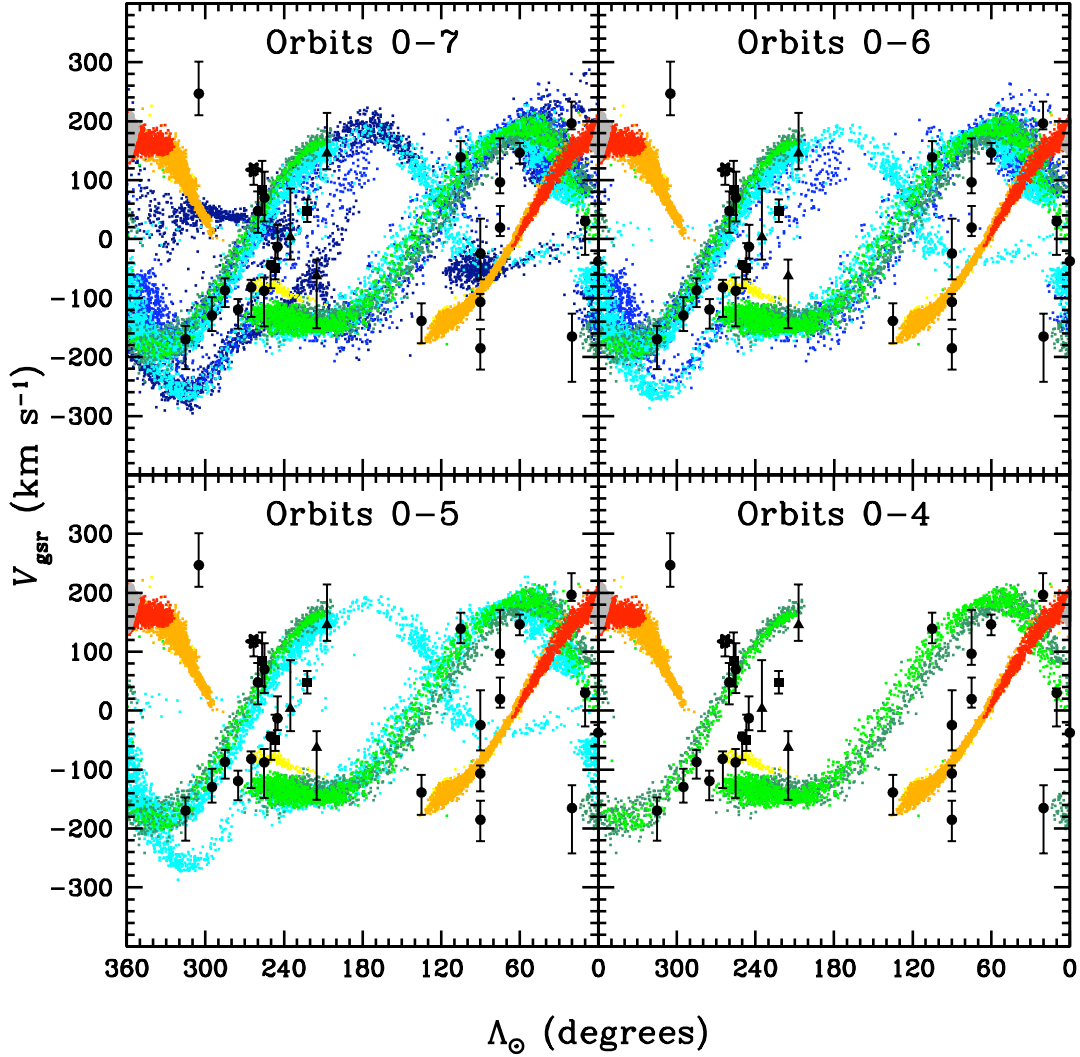
Figure 5.40: Age-limited triaxial halo model and secondary velocity peaks. The Galactic standard of rest radial velocities for the triaxial halo model stars that satisfy the distance cut (described in Section 5.2.2.3) are shown as a function of their Sgr longitude. The four panels sequentially exclude the debris lost during the single oldest orbit remaining in the previous panel. Specifically, the upper left panel excludes the oldest (6.9–7.8 Gyr) debris from the eighth (purple) orbit. The upper right panel additionally excludes debris lost 6.0–6.9 Gyr ago during the seventh (navy blue) orbit. The lower left panel additionally excludes debris lost 5.1–6.0 Gyr ago during the sixth (blue) orbit. Finally, the lower right panel additionally excludes debris lost 4.2–5.0 Gyr ago during the fifth (cyan) orbit. This panel includes currently bound stars (grey), debris lost over the current orbit (red, 0–0.5 Gyr), and the four previous orbits (orange, 0.5–1.3 Gyr; yellow, 1.4–2.3 Gyr; green, 2.4–3.2 Gyr; and dark green, 3.2–4.2 Gyr). The range of included orbits are listed near the top of each panel. The black data points with asymmetric error bars are plotted at the $(\Lambda_{\odot}, V_{\mathrm{peak2}})$ values (see Table 5.2) for the 30 fields in our survey that contained an identified secondary velocity peak. The same symbols as in the previous secondary velocity peak plots are used.
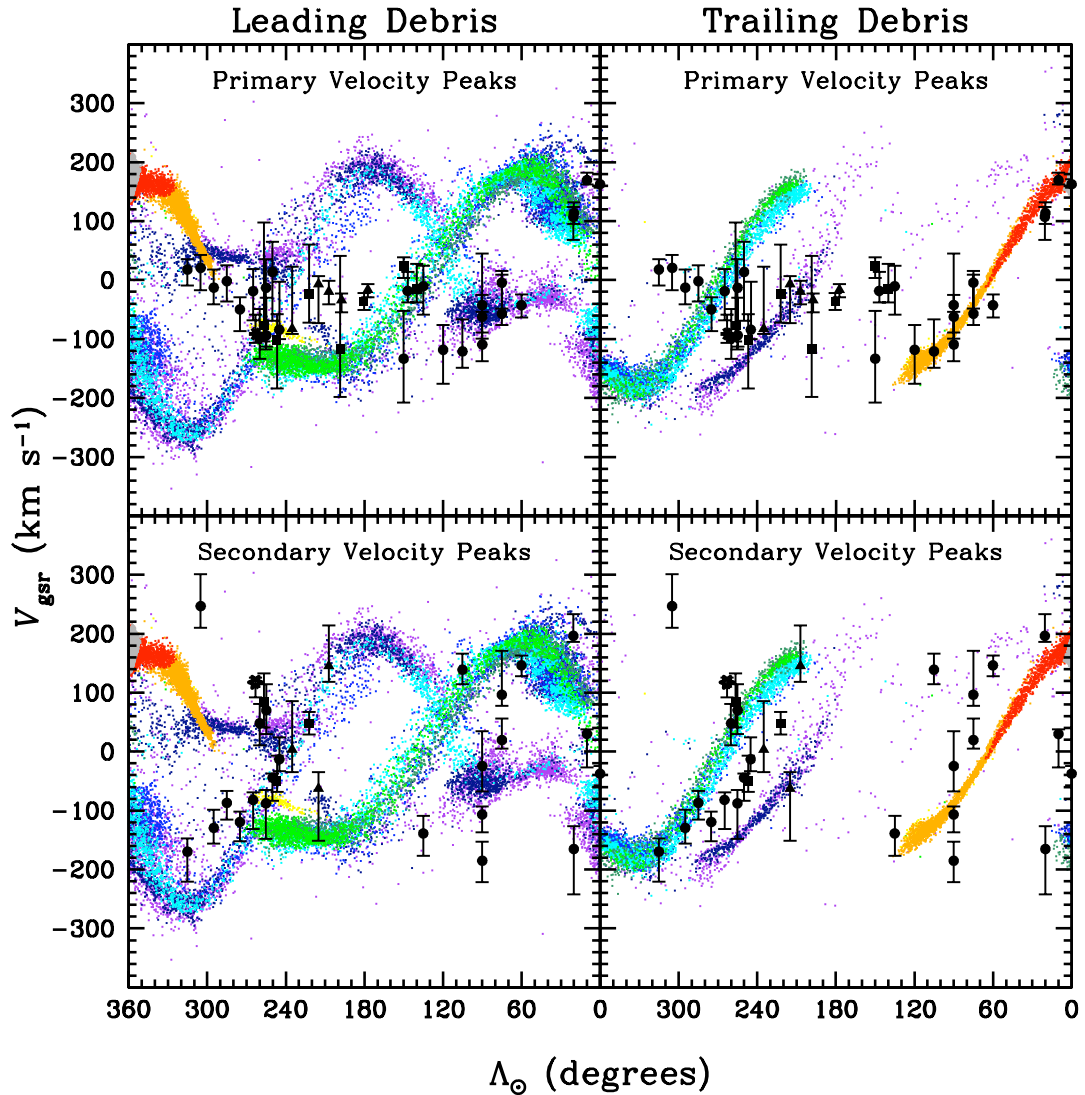
Figure 5.41: Comparisons of velocity peaks to leading and trailing Sgr debris. The Galactic standard of rest radial velocities for the triaxial halo model stars that satisfy the distance cut (described in Section 5.2.2.3) are shown as a function of their Sgr longitude. The left panels exclusively show the leading stream model debris, while the right panels exclusively show the trailing stream model debris, as indicated by the labels along the top of the figure. The model stars are color-coded as before to indicate on which orbit they became unbound from the core of Sgr. The black data points in the upper panels plot the $(\Lambda_\odot, V_{\mathrm{peak}})$ values for the 39 fields in our survey. The black data points in the lower panels plot the $(\Lambda_\odot, V_{\mathrm{peak2}})$ values for the 30 fields in our survey that contained an identified secondary velocity peak. Asymmetric error bars (as discussed in Section 5.1) are included for each observation. The peak velocities and the lengths of the error bars are listed for every field in Table 5.2. Labels at the top of each panel indicate whether the data points are for the primary or secondary velocity peaks.

CHAPTER 6

Summary and Conclusions

6.1 Summary

In this dissertation we have presented the product of years of work acquiring, reducing, and analyzing the enormous amount of photometric and spectroscopic data that comprise our full 360° study of Sgr and its impressive tidal streams. In this section we summarize the principal issues and significant results covered in each chapter of the dissertation.

Chapter 1 contains the introduction to the dissertation. We began by first describing the nature of halo substructure, and then recounting the initial discovery of the Sagittarius dwarf spheroidal galaxy (Sgr), the closest confirmed dwarf galaxy to the Milky Way. After a description of how gravitational tidal forces lead to the formation of leading and trailing stellar streams, we discussed how observations of the positions and motions of the stars that comprise the streams can be used to constrain the shape of the host galaxy's halo. Since it is necessary to rely on models to interpret these observations, we included a brief summary detailing the way such systems are typical modeled – as an N-body system of particles orbiting in the static potential of the host galaxy. We then provided a chronological review of the relevant literature,

with a particular focus on the observational and modeling efforts that have made significant contributions to, or helped advance, our understanding of the shape of the Milky Way's dark matter halo. The first chapter concluded with a general overview of the dissertation.

Chapter 2 covered the photometric component of the survey. We began the chapter by explaining how our field locations were selected, and we provided maps of the fields in various coordinate systems (Figures 2.1 to 2.3). We then described the acquisition of all of the photometric data. The majority of fields (28) were imaged with IMACS on the Baade 6.5 m telescope at Las Camapnas Observatory. A selection of other instruments were used to acquire the remaining photometry, including: MDM2.4+8K (6 fields), CTIO4m+MosaicII (5 fields), and CTIO4m+BTC (1 field). We then described how the photometric data was reduced using standard IRAF procedures, and how probable main-sequence stars were selected for spectroscopic follow-up from instrumental $(I, V - I)$ color magnitude diagrams (CMDs). Chapter 2 concluded with an explanation of how the Sloan Digital Sky Survey (SDSS) was used to calibrate the photometry, and how the corrections for atmospheric extinction and interstellar reddening were applied. Dereddened CMDs for all of the fields were presented at the end of the Chapter (Figures 2.10 to 2.19).

Chapter 3 covered the spectroscopic component of the survey. The vast majority of the spectroscopy (34 fields) was acquired with the multi-slit spectrograph IMACS. The chapter begins with a detailed explanation of the process by which the multi-slit masks were designed and a summary of the IMACS spectroscopic ob-

serving procedure. A thorough discussion of the IMACS data reduction process was then provided. The COSMOS software package was used to extract combined, two-dimensional, wavelength calibrated spectra from the raw data. Standard IRAF procedures were then used to collapse the spectra down to one dimension and measure each object's radial velocities by cross-correlating them against a synthetic stellar template spectrum. A description of the adopted galactic standard of rest (gsr) velocity reference frame, and its usefulness, were given. Attention was then turned to the Hectospec multi-fiber spectrograph, which was responsible for acquiring the spectra in six northern hemisphere fields. After a brief discussion of the preparations necessary before observing with Hectospec, a short description of the observing procedure was given. A detailed review of the data reduction method, which relied on standard IRAF procedures to process, extract, wavelength calibrate, combine, and ultimately measure radial velocities for each object spectrum was provided.

Chapter 3 continued with a comprehensive analysis of the errors and uncertainties in our radial velocity measurements. Repeat observations were used to develop independent error models for the IMACS and Hectospec data sets that relate the Tonry-Davis statistic (R_{TD}, a quantity measured by the IRAF task `fxcor`, which provides an estimate of the reliability of a Fourier cross-correlation velocity measurement) to the velocity measurement uncertainty, σ_V. These repeat observations were then analyzed more fully. While the Hectospec observations (which were drawn from the multiple exposures of specific fields) were found to be stable, the IMACS fields (which consisted of truly repeated observations) showed signs of zero-point offsets

ranging from $\sim 8 - 16$ km s^{-1}. Numerous efforts to determine the source of the off-sets and to correct for them failed. Ultimately the offsets were incorporated in to the IMACS error model, resulting in artificially inflated uncertainties. In general, the Hectospec velocity measurement uncertainties were significantly lower than the IMACS uncertainties due to the presence of these zero-point offsets and the fact that the Hectospec candidate stars were brighter on average. Comparisons of our measured velocities to those from the SDSS, for the few objects both had in common, showed general agreement between the two down to $I_0 \sim 20$, at which point the differences began to increase rapidly. The Hectospec observation of the radial velocity standard field SA 57 produced velocities in excellent agreement with the published values. Chapter 3 concluded with a discussion of the sequential quality control steps instituted to remove unreliable velocity measurements from the final data set used for analysis. Tables listing the target identifier, equatorial coordinates, dereddened magnitude and color, heliocentric and gsr velocity, velocity measurement uncertainty, and R_{TD} value for every object in every field were included at the end of Chapter 3.

Chapter 4 focused on one particular field in the constellation of Virgo where halo substructure had recently been discovered. Some oblate models for the shape of the Milky Way's dark matter halo predicted that the leading stream of Sgr debris should pass through this volume, with highly negative radial velocities, as it descends on to, and through, the Galactic plane. In Chapter 4 we described the kinematic study we carried out to test this hypothesis. The chapter began with a comprehensive literature review, including a discussion of every observational and theoretical study of

363

the identified substructure in Virgo. A summary of the observational procedure and data reduction process was then given. In total, IMACS spectra were acquired for 111 stars in Virgo and for an additional 60 stars in a control field. In the subsequent analysis and discussion sections several interesting results were presented. No significant kinematic peaks were found in the velocity distribution of the control field, which was consistent with the expectations for a smooth halo population. The Virgo field, however, contained a primary peak in its velocity distribution at -75 km s^{-1}, and a secondary peak at 137 km s^{-1}. The velocity of the secondary peak, which consists primarily of brighter, closer, stars, is consistent with the measured velocity of the Virgo Stellar Stream (VSS) as reported in numerous other studies. The primary velocity peak, which consists mostly of fainter, more distant ($\sim$15–30 kpc) stars, was found to be inconsistent with the oblate halo model predictions that sought to assign the Virgo feature to Sgr. Instead, the primary velocity peak was found to be in excellent agreement with the Law & Majewski (2010) model for the destruction of Sgr in a triaxial halo (or, if axisymmetry is imposed, the prolate halo model of Law et al. (2005) is preferred). Our distance estimates for these stars, however, place them closer than the models suggest ($\sim$35–45 kpc). Ultimately, we concluded that while the leading stream of Sgr is present in the background behind the nominal Virgo Overdensity, the bulk of the halo substructure in Virgo is likely unrelated to Sgr.

In Chapter 5 we first described how the velocity distribution profiles were generated for every field. Of the 34 IMACS fields and 6 Hectospec fields, one IMACS and one Hectospec field had to be eliminated from the data set because they did not

contain useful object spectra (due to either poor weather or inaccurate astrometry). The remaining 38 fields, when combined with the Virgo field, yielded a final kinematic data set consisting of velocity measurements for 2368 unique stars in 39 fields. The velocity distributions for all of these fields were provided in Figures 5.3 to 5.12. The primary, secondary, and tertiary peaks in each of these figures were marked and labeled, and then listed in Table 5.2. Some statistical measures of the asymmetry in each field's velocity distribution were then defined, calculated, and presented in tabular and graphical form.

In the second section of Chapter 5 we compared the results of our survey to the predictions of published models of the destruction of Sgr in Milky Way halos of various shapes. After a brief description of the models and their basic characteristics, we compared their predictions for the locations of Sgr debris with the coordinates of our targeted fields. We then used the technique of photometric parallax to estimate the distances to our survey stars. This information allowed us to estimate the maximum distance probed in each field, and to thus exclude model stars beyond those limits by applying a $\Lambda_\odot$-dependent distance cut to the models. The chapter concluded with a detailed analysis of how well the observed primary and secondary kinematic peaks compared to the predictions of the models. While none of the models were a perfect match, the triaxial model was best able to reproduce the observed velocities, followed closely by the prolate model. The spherical model provided a rather poor match to the observations, and the oblate model was worst in almost every way. The discussion

in the following section includes more detailed conclusions derived from the analysis presented in Section 5.2.3.

6.2 Conclusions

Several significant conclusions can be drawn from the comparisons made in Section 5.2.3 between the kinematic results of our Sgr stream survey and the predictions of the oblate, spherical, prolate, and triaxial halo models. First, the initial $\sim$135° of the trailing stream $(0 < \Lambda_\odot < 135°)$ contains dynamically young debris with a radial velocity trend that is identical in all four models (see Figures 5.24 to 5.28). One might conclude that velocity measurements along this segment of the stream therefore have little or no ability to discriminate between the various models. This misperception, however, ignores the substantial contribution of the extended leading stream debris in these fields, whose predicted velocities vary greatly between the tested models.

This was demonstrated quite nicely in the fields at $\Lambda_\odot$=20° (see Figure 5.31), where the velocity distribution predicted by the triaxial model is the only one consistent with the observations due to the contribution from the older leading stream debris, 340° away from the core. This one particular example, along a portion of the stream long thought to have little diagnostic power, serves to highlight a number of the unique advantages that make our kinematic survey superior to its predecessors. Specifically, the apparent detection of the older, more distant leading stream debris in these fields would have been unlikely, if not impossible, had our survey not: (1) measured velocities for dozens of stars (139 to be exact) at this location, (2) probed distances beyond $\sim$30 kpc, where these particular leading stream stars apparently re-

side, and (3) selected for study the especially populous and long-lived main-sequence stars, which are the only tracers capable of providing the numbers per field necessary for (1) and are also the only stellar population capable of tracing the oldest segments of the stream.

The extended leading stream was also detected in four fields about $\sim$215° away from the core (135° $< \Lambda_\odot <$ 150°). The observed peak velocities in these fields strongly favored the triaxial model. Of the axisymmetric models, the predictions of the prolate model were consistent with the observations, but the spherical and oblate models were not.

It is the young leading stream, however, that is best capable of discriminating between the four models. In the oblate and spherical halo models the leading stream velocities are predicted to plunge to highly negative values ($\lesssim$–200 km s^{-1}) near $\Lambda_\odot \sim$ 270°. This is clearly not observed in the data. Instead the observations show the velocity gradient flattening out in this area at a velocity of $\sim$–100 km s^{-1}. This is best matched by the triaxial model results, and, to a lesser extent, the prolate model results (which go a bit more negative than the triaxial model).

This result was first seen in the Virgo field (Chapter 4), located at $\Lambda_\odot \sim$ 263°. The same result was also seen in Figures 5.24 to 5.28, but Figure 5.32 illustrates the stated conclusions most clearly. The conspicuous failures of the oblate and spherical models to reproduce the observed location and dispersion of the primary peak, as well as the relative heights of the primary and secondary peaks, is unmistakable and disqualifying. The prolate model provides a significantly better match to the

observations in all respects, but an offset of –45 km s^{-1} relative the observed primary peak persists. The triaxial model provides the best match to the observations, accurately predicting the location and dispersion of the primary peak, as well as its height relative to the secondary peak, but fails in other unique ways.

While the prolate and spherical models predict the location of the secondary velocity peak reasonably well, the triaxial model is the most inaccurate of the four, offset by –65 km s^{-1} relative to its observed value. The most notable failure of the triaxial model though, is in its ability to match the distance estimates to the observed Sgr debris. The triaxial model is the only one to place a majority of the primary peak stars beyond the $\sim$39 kpc observational limit in these fields (see Figure 5.33). Only when this limit was relaxed to 50 kpc did the triaxial model predictions match the observed velocity distribution.

It is clear that all of the tested models have identifiable deficiencies, but some more than others. Despite its shortcomings, based on the entirety of the analysis presented in the previous chapter and summarized in this one, we find the triaxial model to best match the observed radial velocity trends along the Sgr streams. Of the axisymmetric models, the prolate model is clearly the best match. The spherical and oblate halo models, however, fail to reproduce the observed velocity trends, and can be ruled out.

6.3   Directions for the Future

The kinematic survey presented in this dissertation represents a significant step forward in our understanding of the Sgr stream. As the observations of Sgr continue

to grow in number and improve in quality, the need for newer, more sophisticated models, that are capable of reproducing and accurately predicting these future observations intensifies. While the triaxial model of Law & Majewski (2010) represents the current state of the art, it has several known deficiencies, most notably, the overwhelming likelihood that it is dynamically unstable.

The triaxial model proposed by Law & Majewski (2010), which is nearly oblate[1], is oriented with its minor, intermediate, and major axes approximately aligned with the Galactic X, Z, and Y axes[2], respectively. This particular orientation, with the spin vector of the disk aligned with the intermediate axis of a triaxial dark matter halo, is difficult to understand. It is known that orbits around intermediate axes are unstable (Adams et al., 2007; Carpintero & Muzzio, 2012). Furthermore, a recent study by Debattista et al. (2013) demonstrated that a disk can never remain perpendicular to the intermediate axis of a triaxial halo. The disk and halo will reorient themselves with several Gyr so that the intermediate axis of the halo lies approximately in the plane of the disk.

Given this, it seems likely that the triaxial model represents an unphysical contrivance, somewhat analogous to the use of epicycles to explain planetary motions: it does an adequate job of reproducing previous observations, and also possesses some predictive power (which we have confirmed), but its inaccuracy increases as higher order details are tested. Ultimately, what is needed is a physically realistic halo

---

[1]The axis ratios of the gravitational potential are: $(c/a)_\Phi = 0.72$ and $(b/a)_\Phi = 0.99$.

[2]The X-axis is along the line connecting the Sun and the Galactic center, the Y-axis is in the Galactic plane, perpendicular to the X-axis, and the Z-axis is perpendicular to the Galactic plane.

model – one that is not static, but has a depth and shape that are allowed to evolve over time, as ours surely has. And one that takes in to account often overlooked dynamical effects, such as the dynamical friction experienced by the stream progenitor. And one that does not assume a smooth halo potential, but rather one filled with substantial substructure, which, (like the Large Magellanic Cloud, for example) could significantly influence the positions and motions of tidal debris. And one that does not require the Galactic disk to lie within the plane defined by two of the halo's symmetry axes – for simulations have shown this to be an unnecessary constraint (Debattista et al., 2013). Only if the realism of the models continue to improve can we begin to fully understand the streams of Sgr, their bifurcations, and the halo that encompasses them.

In addition to improved models, there are a number of ways to improve upon the existing observational studies of Sgr as well. While the youngest segments of the Sgr stream have been well studied, the older extended portions and wraps of the stream remain largely unidentified. It is the future studies of this kinematically old debris that will be the most impactful, and that will best inform future models. Successfully measuring the locations and motions of the old Sgr debris requires the use of long-lived stars. Main-sequence stars are the only stellar population capable of probing such old debris.

At any given location along the stream, the older debris is most likely secondary in number density relative to the younger debris. This fact underscores the necessity to acquire spectra for many (preferably hundreds) of stars per field. Once again,

this requires the targeting of main-sequence stars, which are the only stellar tracer that can be found with such a high number density per field. With large enough numbers (and small enough velocity measurement uncertainties) one can also hope to accurately measure the velocity dispersions of the multiple kinematic features in each field to further constrain the models. At higher resolutions, metallicities can also be measured, which have the potential to shed more light on the nature of the stream bifurcations.

While it seems that main-sequence stars are the ideal tracer to use for future observational studies of Sgr, they are not without their drawbacks. Distance estimates to main-sequence stars come with fairly sizable uncertainties (see Section 5.2.2.2), which makes them more difficult to constrain or compare to models. They are also relatively dim, and therefore can not probe as far in to the halo as other stellar tracers.

Fortunately, recently developed instruments (such as the multi-fiber spectrograph M2FS (Mateo et al., 2012) on the 6.5 m Clay telescope at the Las Campanas Observatory) offer the ability to acquire high quality spectra for hundreds of main-sequence stars per field out to distances that exceed the $\sim$30 kpc limit typical of this survey, while simultaneously providing the resolution necessary to measure the velocity dispersion of kinematic features and the chemical compositions of individual stars. We hope that the capabilities of the next generation of instrumentation will be fully utilized to overcome the limitations of the past, and thus continue the steady progress that has been made towards a more complete understanding of Sgr and the dark halo in which it resides.

REFERENCES

Abazajian, K. N., Adelman-McCarthy, J. K., Agüeros, M. A., Allam, S. S., Allende Prieto, C., An, D., Anderson, K. S. J., Anderson, S. F., Annis, J., Bahcall, N. A., & et al. 2009, ApJS, 182, 543

Adams, F. C., Bloch, A. M., Butler, S. C., Druce, J. M., & Ketchum, J. A. 2007, ApJ, 670, 1027

Adelman-McCarthy, J. K., Agüeros, M. A., Allam, S. S., Anderson, K. S. J., Anderson, S. F., Annis, J., Bahcall, N. A., Bailer-Jones, C. A. L., Baldry, I. K., Barentine, J. C., Beers, T. C., Belokurov, V., Berlind, A., Bernardi, M., Blanton, M. R., Bochanski, J. J., Boroski, W. N., Bramich, D. M., Brewington, H. J., Brinchmann, J., Brinkmann, J., Brunner, R. J., Budavári, T., Carey, L. N., Carliles, S., Carr, M. A., Castander, F. J., Connolly, A. J., Cool, R. J., Cunha, C. E., Csabai, I., Dalcanton, J. J., Doi, M., Eisenstein, D. J., Evans, M. L., Evans, N. W., Fan, X., Finkbeiner, D. P., Friedman, S. D., Frieman, J. A., Fukugita, M., Gillespie, B., Gilmore, G., Glazebrook, K., Gray, J., Grebel, E. K., Gunn, J. E., de Haas, E., Hall, P. B., Harvanek, M., Hawley, S. L., Hayes, J., Heckman, T. M., Hendry, J. S., Hennessy, G. S., Hindsley, R. B., Hirata, C. M., Hogan, C. J., Hogg, D. W., Holtzman, J. A., Ichikawa, S.-i., Ichikawa, T., Ivezić, Ž., Jester, S., Johnston, D. E., Jorgensen, A. M., Jurić, M., Kauffmann, G., Kent, S. M., Kleinman, S. J., Knapp, G. R., Kniazev, A. Y., Kron, R. G., Krzesinski, J., Kuropatkin, N., Lamb, D. Q., Lampeitl, H., Lee, B. C., Leger, R. F., Lima, M., Lin, H., Long, D. C., Loveday, J., Lupton, R. H., Mandelbaum, R., Margon, B., Martínez-Delgado, D., Matsubara, T., McGehee, P. M., McKay, T. A., Meiksin, A., Munn, J. A., Nakajima, R., Nash, T., Neilsen, Jr., E. H., Newberg, H. J., Nichol, R. C., Nieto-Santisteban, M., Nitta, A., Oyaizu, H., Okamura, S., Ostriker, J. P., Padmanabhan, N., Park, C., Peoples, Jr., J., Pier, J. R., Pope, A. C., Pourbaix, D., Quinn, T. R., Raddick, M. J., Re Fiorentin, P., Richards, G. T., Richmond, M. W., Rix, H.-W., Rockosi, C. M., Schlegel, D. J., Schneider, D. P., Scranton, R., Seljak, U., Sheldon, E., Shimasaku, K., Silvestri, N. M., Smith, J. A., Smolčić, V., Snedden, S. A., Stebbins, A., Stoughton, C., Strauss, M. A., SubbaRao, M., Suto, Y., Szalay, A. S., Szapudi, I., Szkody, P., Tegmark, M., Thakar, A. R., Tremonti, C. A., Tucker, D. L., Uomoto, A., Vanden Berk, D. E., Vandenberg, J., Vidrih, S., Vogeley, M. S., Voges, W., Vogt, N. P., Weinberg, D. H., West, A. A., White, S. D. M., Wilhite, B., Yanny, B., Yocum, D. R., York, D. G., Zehavi, I., Zibetti, S., & Zucker, D. B. 2007, ApJS, 172, 634

Ahn, C. P., Alexandroff, R., Allende Prieto, C., Anderson, S. F., Anderton, T., Andrews, B. H., Aubourg, É., Bailey, S., Balbinot, E., Barnes, R., & et al. 2012, ApJS, 203, 21

Ahn, C. P., Alexandroff, R., Allende Prieto, C., Anders, F., Anderson, S. F., Anderton, T., Andrews, B. H., Aubourg, É., Bailey, S., Bastien, F. A., & et al. 2013, ArXiv e-prints

Aihara, H., Allende Prieto, C., An, D., Anderson, S. F., Aubourg, É., Balbinot, E., Beers, T. C., Berlind, A. A., Bickerton, S. J., Bizyaev, D., Blanton, M. R., Bochanski, J. J., Bolton, A. S., Bovy, J., Brandt, W. N., Brinkmann, J., Brown, P. J., Brownstein, J. R., Busca, N. G., Campbell, H., Carr, M. A., Chen, Y., Chiappini, C., Comparat, J., Connolly, N., Cortes, M., Croft, R. A. C., Cuesta, A. J., da Costa, L. N., Davenport, J. R. A., Dawson, K., Dhital, S., Ealet, A., Ebelke, G. L., Edmondson, E. M., Eisenstein, D. J., Escoffier, S., Esposito, M., Evans, M. L., Fan, X., Femenía Castellá, B., Font-Ribera, A., Frinchaboy, P. M., Ge, J., Gillespie, B. A., Gilmore, G., González Hernández, J. I., Gott, J. R., Gould, A., Grebel, E. K., Gunn, J. E., Hamilton, J.-C., Harding, P., Harris, D. W., Hawley, S. L., Hearty, F. R., Ho, S., Hogg, D. W., Holtzman, J. A., Honscheid, K., Inada, N., Ivans, I. I., Jiang, L., Johnson, J. A., Jordan, C., Jordan, W. P., Kazin, E. A., Kirkby, D., Klaene, M. A., Knapp, G. R., Kneib, J.-P., Kochanek, C. S., Koesterke, L., Kollmeier, J. A., Kron, R. G., Lampeitl, H., Lang, D., Le Goff, J.-M., Lee, Y. S., Lin, Y.-T., Long, D. C., Loomis, C. P., Lucatello, S., Lundgren, B., Lupton, R. H., Ma, Z., MacDonald, N., Mahadevan, S., Maia, M. A. G., Makler, M., Malanushenko, E., Malanushenko, V., Mandelbaum, R., Maraston, C., Margala, D., Masters, K. L., McBride, C. K., McGehee, P. M., McGreer, I. D., Ménard, B., Miralda-Escudé, J., Morrison, H. L., Mullally, F., Muna, D., Munn, J. A., Murayama, H., Myers, A. D., Naugle, T., Neto, A. F., Nguyen, D. C., Nichol, R. C., O'Connell, R. W., Ogando, R. L. C., Olmstead, M. D., Oravetz, D. J., Padmanabhan, N., Palanque-Delabrouille, N., Pan, K., Pandey, P., Pâris, I., Percival, W. J., Petitjean, P., Pfaffenberger, R., Pforr, J., Phleps, S., Pichon, C., Pieri, M. M., Prada, F., Price-Whelan, A. M., Raddick, M. J., Ramos, B. H. F., Reylé, C., Rich, J., Richards, G. T., Rix, H.-W., Robin, A. C., Rocha-Pinto, H. J., Rockosi, C. M., Roe, N. A., Rollinde, E., Ross, A. J., Ross, N. P., Rossetto, B. M., Sánchez, A. G., Sayres, C., Schlegel, D. J., Schlesinger, K. J., Schmidt, S. J., Schneider, D. P., Sheldon, E., Shu, Y., Simmerer, J., Simmons, A. E., Sivarani, T., Snedden, S. A., Sobeck, J. S., Steinmetz, M., Strauss, M. A., Szalay, A. S., Tanaka, M., Thakar, A. R., Thomas, D., Tinker, J. L., Tofflemire, B. M., Tojeiro, R., Tremonti, C. A., Vandenberg, J., Vargas Magaña, M., Verde, L., Vogt, N. P., Wake, D. A., Wang, J., Weaver, B. A., Weinberg, D. H., White, M., White, S. D. M., Yanny, B., Yasuda, N., Yeche, C., & Zehavi, I. 2011, ApJS, 193, 29

Beers, T. C., Flynn, K., & Gebhardt, K. 1990, AJ, 100, 32

Belokurov, V., Zucker, D. B., Evans, N. W., Gilmore, G., Vidrih, S., Bramich, D. M., Newberg, H. J., Wyse, R. F. G., Irwin, M. J., Fellhauer, M., Hewett, P. C., Walton,

N. A., Wilkinson, M. I., Cole, N., Yanny, B., Rockosi, C. M., Beers, T. C., Bell, E. F., Brinkmann, J., Ivezić, Ž., & Lupton, R. 2006, ApJ, 642, L137

Bessell, M. S. 1979, PASP, 91, 589

Brink, T. G., Mateo, M., & Martínez-Delgado, D. 2010, AJ, 140, 1337

Bullock, J. S., & Johnston, K. V. 2005, ApJ, 635, 931

Carpintero, D. D., & Muzzio, J. C. 2012, Celestial Mechanics and Dynamical Astronomy, 112, 107

Carroll, B. W., & Ostlie, D. A. 1996, An Introduction to Modern Astrophysics (Reading, MA: Addison-Wesley)

Chou, M., Majewski, S. R., Cunha, K., Smith, V. V., Patterson, R. J., Martínez-Delgado, D., Law, D. R., Crane, J. D., Muñoz, R. R., Garcia López, R., Geisler, D., & Skrutskie, M. F. 2007, ApJ, 670, 346

Coelho, P., Barbuy, B., Meléndez, J., Schiavon, R. P., & Castilho, B. V. 2005, A&A, 443, 735

Debattista, V. P., Roškar, R., Valluri, M., Quinn, T., Moore, B., & Wadsley, J. 2013, MNRAS, 434, 2971

Deg, N., & Widrow, L. 2013, MNRAS, 428, 912

Dehnen, W., & Binney, J. J. 1998, MNRAS, 298, 387

Dohm-Palmer, R. C., Helmi, A., Morrison, H., Mateo, M., Olszewski, E. W., Harding, P., Freeman, K. C., Norris, J., & Shectman, S. A. 2001, ApJ, 555, L37

Dressler, A., Bigelow, B., Hare, T., Sutin, B., Thompson, I., Burley, G., Epps, H., Oemler, A., Bagish, A., Birk, C., Clardy, K., Gunnels, S., Kelson, D., Shectman, S., & Osip, D. 2011, PASP, 123, 288

Ducati, J. R., Bevilacqua, C. M., Rembold, S. B., & Ribeiro, D. 2001, ApJ, 558, 309

Duffau, S., Zinn, R., Vivas, A. K., Carraro, G., Méndez, R. A., Winnick, R., & Gallart, C. 2006, ApJ, 636, L97

Edelsohn, D. J., & Elmegreen, B. G. 1997, MNRAS, 290, 7

Fabricant, D., Fata, R., Roll, J., Hertz, E., Caldwell, N., Gauron, T., Geary, J., McLeod, B., Szentgyorgyi, A., Zajac, J., Kurtz, M., Barberis, J., Bergner, H., Brown, W., Conroy, M., Eng, R., Geller, M., Goddard, R., Honsa, M., Mueller, M., Mink, D., Ordway, M., Tokarz, S., Woods, D., Wyatt, W., Epps, H., & Dell'Antonio, I. 2005, PASP, 117, 1411

Fellhauer, M., Belokurov, V., Evans, N. W., Wilkinson, M. I., Zucker, D. B., Gilmore, G., Irwin, M. J., Bramich, D. M., Vidrih, S., Wyse, R. F. G., Beers, T. C., & Brinkmann, J. 2006, ApJ, 651, 167

Gómez-Flechoso, M. A., Fux, R., & Martinet, L. 1999, A&A, 347, 77

Helmi, A. 2004a, PASA, 21, 212

—. 2004b, ApJ, 610, L97

Helmi, A., & White, S. D. M. 2001, MNRAS, 323, 529

Hernquist, L. 1990, ApJ, 356, 359

Horne, K. 1986, PASP, 98, 609

Ibata, R., Irwin, M., Lewis, G., Ferguson, A. M. N., & Tanvir, N. 2001a, Nature, 412, 49

Ibata, R., Irwin, M., Lewis, G. F., & Stolte, A. 2001b, ApJ, 547, L133

Ibata, R., Lewis, G. F., Irwin, M., Totten, E., & Quinn, T. 2001c, ApJ, 551, 294

Ibata, R., Lewis, G. F., Martin, N. F., Bellazzini, M., & Correnti, M. 2013, ApJ, 765, L15

Ibata, R., Martin, N. F., Irwin, M., Chapman, S., Ferguson, A. M. N., Lewis, G. F., & McConnachie, A. W. 2007, ApJ, 671, 1591

Ibata, R. A., Gilmore, G., & Irwin, M. J. 1994, Nature, 370, 194

—. 1995, MNRAS, 277, 781

Ibata, R. A., & Lewis, G. F. 1998, ApJ, 500, 575

Ibata, R. A., Wyse, R. F. G., Gilmore, G., Irwin, M. J., & Suntzeff, N. B. 1997, AJ, 113, 634

Jiang, I.-G., & Binney, J. 2000, MNRAS, 314, 468

Johnston, K. V., Law, D. R., & Majewski, S. R. 2005, ApJ, 619, 800

Johnston, K. V., Majewski, S. R., Siegel, M. H., Reid, I. N., & Kunkel, W. E. 1999, AJ, 118, 1719

Johnston, K. V., Spergel, D. N., & Hernquist, L. 1995, ApJ, 451, 598

Jordi, K., Grebel, E. K., & Ammon, K. 2006, A&A, 460, 339

Jurić, M., Ivezić, Ž., Brooks, A., Lupton, R. H., Schlegel, D., Finkbeiner, D., Padmanabhan, N., Bond, N., Sesar, B., Rockosi, C. M., Knapp, G. R., Gunn, J. E., Sumi, T., Schneider, D. P., Barentine, J. C., Brewington, H. J., Brinkmann, J., Fukugita, M., Harvanek, M., Kleinman, S. J., Krzesinski, J., Long, D., Neilsen, Jr., E. H., Nitta, A., Snedden, S. A., & York, D. G. 2008, ApJ, 673, 864

Keller, S. C. 2010, PASA, 27, 45

Keller, S. C., da Costa, G. S., & Prior, S. L. 2009, MNRAS, 394, 1045

Keller, S. C., Murphy, S., Prior, S., Da Costa, G., & Schmidt, B. 2008, ApJ, 678, 851

Kelson, D. D. 2003, PASP, 115, 688

King, I. R. 1966, AJ, 71, 64

Kunder, A., & Chaboyer, B. 2009, AJ, 137, 4478

Kundu, A., Majewski, S. R., Rhee, J., Rocha-Pinto, H. J., Polak, A. A., Slesnick, C. L., Kunkel, W. E., Johnston, K. V., Patterson, R. J., Geisler, D., Gieren, W., Seguel, J., Smith, V. V., Palma, C., Arenas, J., Crane, J. D., & Hummels, C. B. 2002, ApJ, 576, L125

Law, D. R., Johnston, K. V., & Majewski, S. R. 2005, ApJ, 619, 807 (LJM05)

Law, D. R., & Majewski, S. R. 2010, ApJ, 714, 229 (LM10)

Law, D. R., Majewski, S. R., & Johnston, K. V. 2009, ApJ, 703, L67

Law, D. R., Majewski, S. R., Skrutskie, M. F., & Johnston, K. V. 2004, in Astronomical Society of the Pacific Conference Series, Vol. 327, Satellites and Tidal Streams, ed. F. Prada, D. Martinez Delgado, & T. J. Mahoney, 239

Majewski, S. R., Siegel, M. H., Kunkel, W. E., Reid, I. N., Johnston, K. V., Thompson, I. B., Landolt, A. U., & Palma, C. 1999, AJ, 118, 1709

Majewski, S. R., Skrutskie, M. F., Weinberg, M. D., & Ostheimer, J. C. 2003, ApJ, 599, 1082

Majewski, S. R., Kunkel, W. E., Law, D. R., Patterson, R. J., Polak, A. A., Rocha-Pinto, H. J., Crane, J. D., Frinchaboy, P. M., Hummels, C. B., Johnston, K. V., Rhee, J., Skrutskie, M. F., & Weinberg, M. 2004, AJ, 128, 245

Martínez-Delgado, D., Aparicio, A., Gómez-Flechoso, M. Á., & Carrera, R. 2001, ApJ, 549, L199

Martínez-Delgado, D., Gómez-Flechoso, M. Á., Aparicio, A., & Carrera, R. 2004, ApJ, 601, 242

Martínez-Delgado, D., Peñarrubia, J., Gabany, R. J., Trujillo, I., Majewski, S. R., & Pohlen, M. 2008, ApJ, 689, 184

Martínez-Delgado, D., Peñarrubia, J., Jurić, M., Alfaro, E. J., & Ivezić, Z. 2007, ApJ, 660, 1264

Martínez-Delgado, D., Pohlen, M., Gabany, R. J., Majewski, S. R., Peñarrubia, J., & Palma, C. 2009, ApJ, 692, 955

Martínez-Delgado, D., Gabany, R. J., Crawford, K., Zibetti, S., Majewski, S. R., Rix, H.-W., Fliri, J., Carballo-Bello, J. A., Bardalez-Gagliuffi, D. C., Peñarrubia, J., Chonis, T. S., Madore, B., Trujillo, I., Schirmer, M., & McDavid, D. A. 2010, AJ, 140, 962

Mateo, M., Bailey, J. I., Crane, J., Shectman, S., Thompson, I., Roederer, I., Bigelow, B., & Gunnels, S. 2012, in Society of Photo-Optical Instrumentation Engineers (SPIE) Conference Series, Vol. 8446, Society of Photo-Optical Instrumentation Engineers (SPIE) Conference Series

Mateo, M., Olszewski, E. W., & Morrison, H. L. 1998, ApJ, 508, L55

Miskolczi, A., Bomans, D. J., & Dettmar, R.-J. 2011, A&A, 536, A66

Miyamoto, M., & Nagai, R. 1975, PASJ, 27, 533

Monaco, L., Bellazzini, M., Bonifacio, P., Buzzoni, A., Ferraro, F. R., Marconi, G., Sbordone, L., & Zaggia, S. 2007, A&A, 464, 201

Monet, D. G., Levine, S. E., Canzian, B., Ables, H. D., Bird, A. R., Dahn, C. C., Guetter, H. H., Harris, H. C., Henden, A. A., Leggett, S. K., Levison, H. F., Luginbuhl, C. B., Martini, J., Monet, A. K. B., Munn, J. A., Pier, J. R., Rhodes, A. R., Riepe, B., Sell, S., Stone, R. C., Vrba, F. J., Walker, R. L., Westerhout, G., Brucato, R. J., Reid, I. N., Schoening, W., Hartley, M., Read, M. A., & Tritton, S. B. 2003, AJ, 125, 984

Newberg, H. J., Yanny, B., Cole, N., Beers, T. C., Re Fiorentin, P., Schneider, D. P., & Wilhelm, R. 2007, ApJ, 668, 221 (NYC07)

Newberg, H. J., Yanny, B., Rockosi, C., Grebel, E. K., Rix, H., Brinkmann, J., Csabai, I., Hennessy, G., Hindsley, R. B., Ibata, R., Ivezić, Z., Lamb, D., Nash, E. T., Odenkirchen, M., Rave, H. A., Schneider, D. P., Smith, J. A., Stolte, A., & York, D. G. 2002, ApJ, 569, 245

Plummer, H. C. 1911, MNRAS, 71, 460

Prior, S. L., Da Costa, G. S., & Keller, S. C. 2009a, ApJ, 704, 1327

Prior, S. L., Da Costa, G. S., Keller, S. C., & Murphy, S. J. 2009b, ApJ, 691, 306

Robin, A. C., Reylé, C., Derrière, S., & Picaud, S. 2003, A&A, 409, 523 (erratum 416, 157 [2004])

Ruhland, C., Bell, E. F., Rix, H.-W., & Xue, X.-X. 2011, ApJ, 731, 119

Schechter, P. L., Mateo, M., & Saha, A. 1993, PASP, 105, 1342

Schlegel, D. J., Finkbeiner, D. P., & Davis, M. 1998, ApJ, 500, 525

Seabroke, G. M., Gilmore, G., Siebert, A., Bienaymé, O., Binney, J., Bland-Hawthorn, J., Campbell, R., Freeman, K. C., Gibson, B., Grebel, E. K., Helmi, A., Munari, U., Navarro, J. F., Parker, Q. A., Siviero, A., Steinmetz, M., Watson, F. G., Wyse, R. F. G., Zwitter, T., Peñarrubia, J., Smith, M. C., & Williams, M. 2008, MNRAS, 384, 11

Sirko, E., Goodman, J., Knapp, G. R., Brinkmann, J., Ivezić, Ž., Knerr, E. J., Schlegel, D., Schneider, D. P., & York, D. G. 2004, AJ, 127, 899

Starkenburg, E., Helmi, A., Morrison, H. L., Harding, P., van Woerden, H., Mateo, M., Olszewski, E. W., Sivarani, T., Norris, J. E., Freeman, K. C., Shectman, S. A., Dohm-Palmer, R. C., Frey, L., & Oravetz, D. 2009, ApJ, 698, 567

Stefanik, R. P., Latham, D. W., & Davis, R. J. 2006, PASP, 118, 1656

Tonry, J., & Davis, M. 1979, AJ, 84, 1511

Totten, E. J., & Irwin, M. J. 1998, MNRAS, 294, 1

Totten, E. J., Irwin, M. J., & Whitelock, P. A. 2000, MNRAS, 314, 630

Velazquez, H., & White, S. D. M. 1995, MNRAS, 275, L23

Vera-Ciro, C., & Helmi, A. 2013, ApJ, 773, L4

Vivas, A. K., Jaffé, Y. L., Zinn, R., Winnick, R., Duffau, S., & Mateu, C. 2008, AJ, 136, 1645

Vivas, A. K., & Zinn, R. 2003, Mem. Soc. Astron. Ital., 74, 928

—. 2006, AJ, 132, 714

Vivas, A. K., Zinn, R., Andrews, P., Bailyn, C., Baltay, C., Coppi, P., Ellman, N., Girard, T., Rabinowitz, D., Schaefer, B., Shin, J., Snyder, J., Sofia, S., van Altena, W., Abad, C., Bongiovanni, A., Briceño, C., Bruzual, G., Della Prugna, F., Herrera, D., Magris, G., Mateu, J., Pacheco, R., Sánchez, G., Sánchez, G., Schenner, H., Stock, J., Vicente, B., Vieira, K., Ferrín, I., Hernandez, J., Gebhard, M., Honeycutt, R., Mufson, S., Musser, J., & Rengstorf, A. 2001, ApJ, 554, L33

Walker, M. G., Mateo, M., Olszewski, E. W., Bernstein, R., Sen, B., & Woodroofe, M. 2007, ApJS, 171, 389

Walker, M. G., Mateo, M., Olszewski, E. W., Bernstein, R., Wang, X., & Woodroofe, M. 2006, AJ, 131, 2114

Walsh, S. M., Willman, B., & Jerjen, H. 2009, AJ, 137, 450

Yanny, B., Newberg, H. J., Kent, S., Laurent-Muehleisen, S. A., Pier, J. R., Richards, G. T., Stoughton, C., Anderson, Jr., J. E., Annis, J., Brinkmann, J., Chen, B., Csabai, I., Doi, M., Fukugita, M., Hennessy, G. S., Ivezić, Ž., Knapp, G. R., Lupton, R., Munn, J. A., Nash, T., Rockosi, C. M., Schneider, D. P., Smith, J. A., & York, D. G. 2000, ApJ, 540, 825

Yanny, B., Newberg, H. J., Grebel, E. K., Kent, S., Odenkirchen, M., Rockosi, C. M., Schlegel, D., Subbarao, M., Brinkmann, J., Fukugita, M., Ivezic, Ž., Lamb, D. Q., Schneider, D. P., & York, D. G. 2003, ApJ, 588, 824

Yanny, B., Newberg, H. J., Johnson, J. A., Lee, Y. S., Beers, T. C., Bizyaev, D., Brewington, H., Fiorentin, P. R., Harding, P., Malanushenko, E., Malanushenko, V., Oravetz, D., Pan, K., Simmons, A., & Snedden, S. 2009, ApJ, 700, 1282

Zinn, R., Vivas, A. K., Gallart, C., & Winnick, R. 2004, in Astronomical Society of the Pacific Conference Series, Vol. 327, Satellites and Tidal Streams, ed. F. Prada, D. Martinez Delgado, & T. J. Mahoney, 92